

This is an **Accepted Manuscript** version of the following article, published in *Chemical Engineering Journal* by Elsevier:

Lumbaqué, E.C., Radjenovic, J. (2023). Electro-oxidation of persistent organic contaminants at graphene sponge electrodes using intermittent current. *Chemical Engineering Journal*, vol. 476, art.num.146910

Available online at

<https://doi.org/10.1016/j.cej.2023.146910>

© 2023. This manuscript version is made available under the CC-BY-NC-ND 4.0 license <https://creativecommons.org/licenses/by-nc-nd/4.0/>



Electro-oxidation of persistent organic contaminants at graphene sponge electrodes using intermittent current

Elisabeth Cuervo Lumbaque^{a,b}, Jelena Radjenovic^{a,c}

^a*Catalan Institute for Water Research (ICRA), Emili Grahit 101, 17003 Girona, Spain*

^b*University of Girona, Girona, Spain*

^c*Catalan Institution for Research and Advanced Studies (ICREA), Passeig Lluís Companys 23,
08010 Barcelona, Spain*

** Corresponding author:*

Jelena Radjenovic, Catalan Institute for Water Research (ICRA), Emili Grahit 101, 17003 Girona, Spain

Phone: + 34 972 18 33 80; Fax: +34 972 18 32 48; E-mail: jradjenovic@icra.cat

Abstract

Borophene (Bph) and hexagonal boron nitride (hBN)-modified graphene sponge anode coupled to N-doped graphene sponge cathode were applied for electrochemical degradation of persistent organic contaminants using intermittent current. Three different ON-OFF pulse cycles were tested using low-conductivity supporting electrolyte in flow-through mode. Functionalization of the reduced graphene oxide (RGO) with Bph and hBN improved the ability of the double layer to store electrical charge, thus maintaining the generation of H_2O_2 , O_3 , and $\cdot\text{OH}$ even during the OFF cycles. Both anodes tested showed enhanced contaminant removal during shorter OFF periods (e.g. 52.5s/52.s and 75s/30s ON/OFF), due to the improved retention of anode charge during the shorter OFF stages. Electrochemical removal of the target contaminants required 24 kWh m^{-3} in continuous current mode for both hBN-RGO and Bph-RGO anodes at 231 A m^{-2} , which was lowered to 11.7 and 13.5 kWh m^{-3} respectively, using ON-OFF pulse cycles. Electrochemical degradation pathways were elucidated in both systems using carbamazepine as a representative persistent contaminant. Flow-through reactors with both Bph- and hBN-RGO anodes removed $\geq 60\%$ of the target contaminants in a single pass using continuous current, whereas intermittent current led to somewhat decreased removal efficiencies (43-58%) due to the scavenging effect of the wastewater matrix. Thus, halving the current ON time led to less than 20% decrease in the removal efficiencies due to the capacitive properties of RGO. Given that switching to intermittent current decreased the energy consumption from 9.3 kWh m^{-3} to 4.4 kWh m^{-3} (Bph-RGO anode) and from 6.9 kWh m^{-3} to 3.6 kWh m^{-3} (hBN-RGO anode), higher removal of the target contaminants can be achieved by coupling sequential reactors in the intermittent current mode.

Keywords

Graphene-based material; 2D materials; electrooxidation; intermittent current; capacitance.

1. Introduction

Carbon-based, metal-free catalysts such as graphene-based materials have emerged as one of the most promising materials for diverse applications, including water and wastewater treatment and energy storage devices [1,2]. The use of reduced graphene oxide (RGO)-based electrodes in electrochemical units, whether their target application is aiming at supercapacitors and batteries, or (waste)water treatment, offers a range of advantages such as low-cost and easy and scalable fabrication methods, electrochemical stability (even at high current densities), anticorrosive properties and high specific capacitance [2–4]. RGO-based electrodes combine both the capacitive behavior resulting from the electrostatic double-layer capacitance and the pseudocapacitive behavior resulting from the redox reactions, endowed by the presence of hydrophilic, oxygen functional groups separated by the hydrophobic regions, which ensure that the active surface is accessible to the electrolyte [5]. In addition, RGO-based anodes have a demonstrated electrocatalytic activity in aqueous solutions for the degradation of organic and microbial contaminants [2–4,6]. Capacitive properties of graphene can enable significant energy savings in electrochemical water treatment. For example, electrochemical disinfection of tap water with boron (B)-doped graphene sponge anode enabled 5.5 log removal of *E. coli* using both continuous and intermittent current application, but with 76% lower energy consumption in the latter case, which was decreased from 5.70 kWh m⁻³ to 1.38 kWh m⁻³ [2]. Doping of graphene with B and other elements (e.g., nitrogen (N), phosphorus (P)) is a well-known strategy for increasing the capacitance of the material as it facilitates charge accumulation, and enhances further the interaction of the electrode with the electrolyte [1]. Elemental doping of graphene-based electrodes with B and N has also been shown to increase their electrocatalytic activity [3], whereas this

electrocatalytic activity is enhanced even further by introducing a two-dimensional (2D) material such as borophene (Bph) into the RGO coating [6]. Bph-doped graphene sponge anode yielded higher concentrations of oxidant species (e.g., H₂O₂, O₃, ·OH) and enhanced the degradation of persistent organic contaminants compared with the boron-doped graphene sponge anode [3,6]. On the other hand, functionalization of the graphene sponge anode with hBN enhanced the van der Waals and π - π interactions of more hydrophobic contaminants with the electrode surface [6]. It is unclear, however, whether the presence of these 2D materials in graphene-based electrodes endows them with sufficient capacitance to degrade persistent organic contaminants under intermittent current, which would allow to lower the overall energy consumption of the system.

In this study, we evaluated the performance of Bph- and hBN-functionalized graphene sponge anodes, coupled with N-doped graphene sponge cathodes, for electrochemical oxidation of a set of model contaminants known to be persistent to oxidation, i.e., carbamazepine (CBZ), iopromide (IPM), and triclopyr (TCP), performed with different cycles of intermittent anodic current. The objectives of the study were: *i*) to investigate the impact of functionalization with hBN and Bph on the capacitive properties of RGO, *ii*) to investigate the impact of intermittent anodic current on the system performance using different ON-OFF cycles, and *iii*) to identify the pathways of electrochemical degradation of a model contaminant at hBN-RGO and Bph-RGO anode, and *iv*) to demonstrate the system performance in real municipal wastewater effluent. The obtained results prove the feasibility of using graphene-based electrodes functionalized with 2D materials for the removal of organic pollutants in the intermittent current application mode.

2. Materials and methods

2.1 Chemicals and reagents

Graphene oxide (GO) aqueous dispersion (0.4 % w/w) was purchased from Graphenea, Inc (Spain). Analytical grade standards for CBZ, IPM, and TCP, were purchased from Sigma-Aldrich. Acetonitrile, methanol, and water (LC grade) were supplied by Merck and Fisher. All solvents and chemicals used in this study were of analytical grade.

2.2 Experimental set-up

Cylindrical flow-through reactor made of methacrylate was equipped with hBN- or Bph-doped graphene sponge anode and N-doped cathode. Details of the material synthesis and comprehensive material surface characterization are reported in our previous work [3,6]. To avoid short-circuiting of the sandwiched electrodes, anode and cathode were separated by a thin polypropylene membrane. Leak-free Ag/AgCl electrode (LF-1 Harvard Apparatus) was placed in between the anode and the cathode. The experiments were performed using a low-conductivity supporting electrolyte (10 mM Na₂HPO₄/NH₂PO₄, pH 7, 1.1 mS cm⁻¹), in one pass, flow-through mode (anode-cathode flow direction) at a flow rate of 5 mL min⁻¹, resulting in a hydraulic residence time (HRT) of 3.45 min. Anodic current density of 231 A m⁻², calculated using the electrode's projected surface area, was applied using a Biologic VMP-300 potentiostat.

Target contaminants (CBZ, IPM, and TCP) were added to the supporting electrolyte at the initial concentration of 1 μM each. Samples were collected at the outlet of reactor, and immediately quenched with methanol. For intermittent application of anodic current (231 A m⁻²), three different ON-OFF pulse cycles were tested: *i*) symmetrical cycles with 105s ON - 105s OFF, *ii*) symmetrical

cycles of 52.5s ON - 52.5s OFF, and *iii*) asymmetrical cycles with 75s ON - 30s OFF. The ohmic drops were calculated from the data obtained in the electrochemical impedance spectroscopy (EIS) measurements, and the recorded anode potentials were corrected for ohmic drops. The near-vertical slope in the EIS analysis at low frequency was used for obtaining the imaginary part of the double-layer capacitance (C_{dl}), where C_{dl} represents the real capacitance of the cell at the corresponding frequency [7]. Nyquist plots of RGO, hBN-RGO and Bph-RGO anodes were fitted with an equivalent electrical circuit using the BioLogic EC-lab software.

To test the performance of the Bph-RGO and hBN-RGO anodes under more realistic conditions, experiments were performed using a secondary treated municipal wastewater effluent from a wastewater treatment plant (WWTP) in Girona, Spain (**Table S1**), amended with the target pollutants at 1 μM concentration. The experiments were conducted using a continuous current of 115 A m^{-2} , and intermittent current with a symmetrical cycle 52.5 s ON/ 52.5s OFF. To prevent blockage of the graphene sponge electrodes, wastewater effluent was filtered using a 0.22 μm filter. All experiments were conducted in triplicate, and the obtained results are presented as mean values with their respective standard deviations.

2. 3 Analytical methods

Analyses of the target contaminants were performed using Waters Acquity Ultra-PerformanceTM liquid chromatograph (UPLC) coupled to a 5500 QTRAP system (Applied Biosystems), equipped with an electrospray (ESI) source. Details of the analytical methods are summarized in **Text S1** and **Tables S2 and S3**. The concentration of the electrogenerated H_2O_2 was determined by a spectrophotometric method [8]. The concentration of ozone was measured by a photometric test kit (LCK) with the quantification limit of 0.05 mg L^{-1} . Terephthalic acid (TA) was used to evaluate

the formation of hydroxyl radicals ($\cdot\text{OH}$) [2,6]; the steady-state concentration of $\cdot\text{OH}$ was determined using UV-vis spectroscopy at 239 nm and $[\cdot\text{OH}]$ was determined as a ratio of pseudo-first rate constant of TA decay (k_{TA} , s^{-1}) and $k_{\text{TA},\cdot\text{OH}}$ [9].

2.4 Study of the transformation products

To gain insight into the degradation mechanism occurring at the graphene sponge electrodes functionalized with the 2D materials, experiments were performed with the Bph-RGO and hBN-RGO anode at 231 A m^{-2} , and using CBZ as a model compound. Structural elucidation of the transformation products (TPs) was performed with an Orbitrap Exploris 120 mass spectrometer (Thermo Fisher Scientific Inc), using a Hypersil GOLDTM column (50x2.1 mm, particle size 1.9 μ , Thermo fisher). The samples were analyzed in full scan mode, from m/z 100 to 1,000, to identify suspect m/z and further fragment them at a normalized collision energy of 30%. The fragmentation spectra were acquired by Orbitrap working at a resolution of 15,000 to obtain structural information of the suspect TPs. All the data was acquired and processed with Compound DiscovererTM 3.0 Software. Details of the analytical method were summarized in **Text S1**.

3. Results and discussion

3.1 Electrochemical characterization of graphene sponge electrodes

Electrochemical performance of RGO, hBN-RGO and Bph-RGO anode vs N-RGO cathode was investigated by cyclic voltammetry (CV) measurements in 100 mM of phosphate buffer solution between 0 and 0.8 V vs SHE in slow scan rates lead to see the capacitive behavior (i.e., rectangle shape) (**Figure 1 A-C**). The area under the curve of Both hBN and Bph-RGO anode increased with respect to the RGO anode, suggesting an enhanced capacitive behavior of the 2D-

functionalized sponges [10]. This is due to the larger electrochemically active surface areas (S_E) of hBN-RGO ($0.81 \text{ m}^2 \text{ g}^{-1}$), and Bph-RGO ($0.90 \text{ m}^2 \text{ g}^{-1}$) compared to the undoped RGO sponge ($0.67 \text{ m}^2 \text{ g}^{-1}$) [6], which has a direct impact on the increase in capacitance. The larger electrochemically active surface areas of hBN-RGO and Bph-RGO are beneficial for ion migration from electrolyte to the electrode surface, and formation of the double layer, which has an impact on the capacitance of electrode. Conversely, as scan rates increase, the rectangular shapes undergoes modifications, a phenomenon attributed to the presence of defects and oxygen functionalities in RGO-based anodes [6,11]. Also, it is confirmed that addition of borophene caused a deviation from typical rectangular shape due to the presence of faradaic processes occurring at the electrode/electrolyte interface [12].

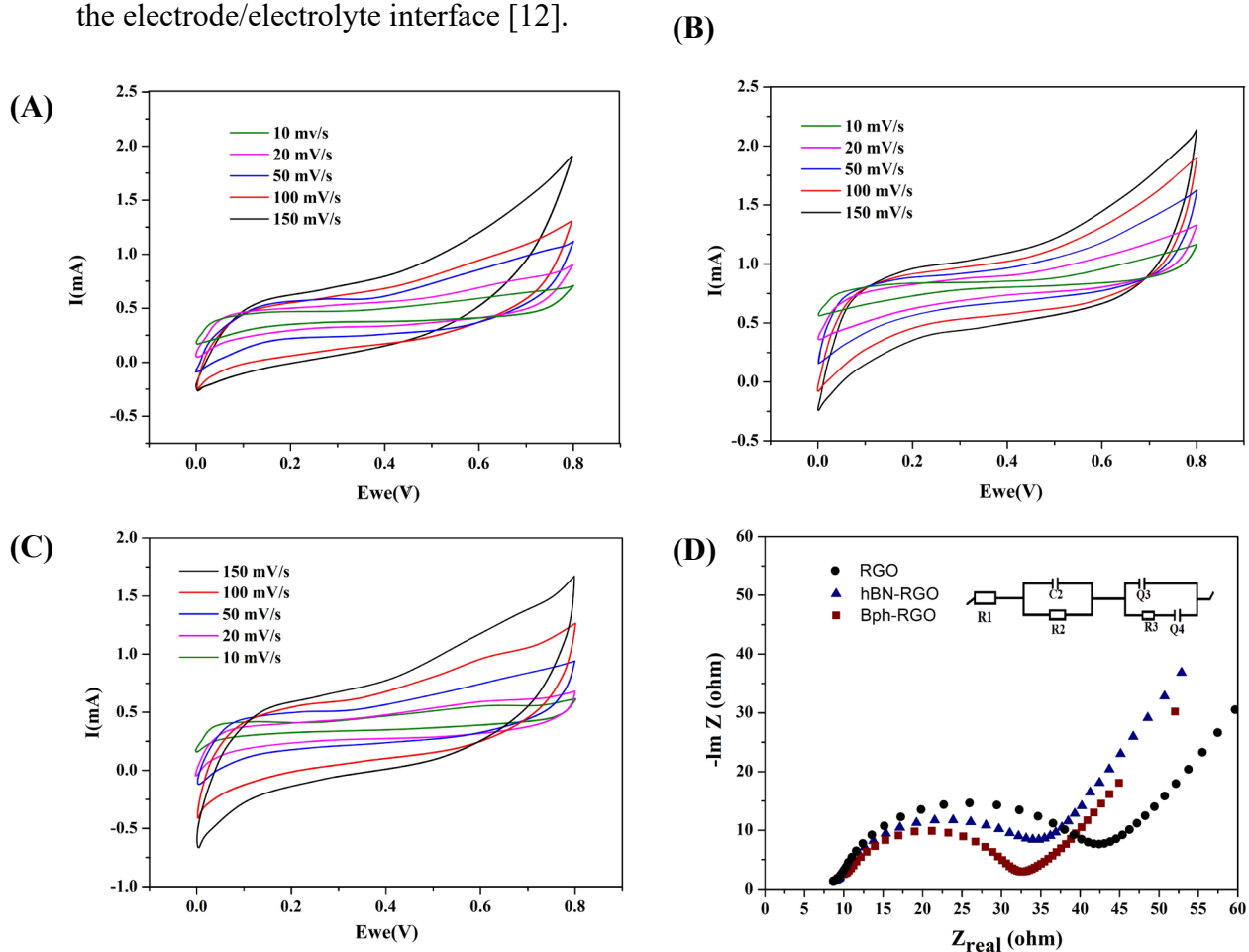


Figure 1. Cyclic voltammetry (CV) scans recorded in 100 mM phosphate buffer at pH 7, scan rate of 10-150 mV/s for: **A)** RGO, **B)** hBN-RGO anode, and **C)** Bph-RGO anode, all coupled to N-

RGO cathode. **D)** Experimental Nyquist plots for all anodes in the low conductivity electrolyte (10 mM phosphate buffer at pH 7, 1 mS cm^{-1}).

To further study the impact of the functionalization of graphene with the 2D materials, we obtained EIS Nyquist plots for RGO, hBN-RGO and Bph-RGO anode in 10 mM phosphate buffer (PB) (**Figure 1D**). The Nyquist plot of a faradaic impedance spectrum across a broad frequency range frequently includes two distinct components. First, there is a semicircle in the region of high- to mid-frequency that represents the frequency region where the electrochemical process is governed by the charge transfer phenomena and double layer resistance at the electrolyte-electrode surface (R_{CT}). Secondly, there is a straight line that signifies the frequency region where the electrochemical process is influenced by the mass transfer phenomena to the electrode surface. The characteristics of these components may vary depending on the specific values of C_{dl} and R_{CT} [13,14]. In the low-frequency domain, all tested anodes exhibit a clear differentiation between the semicircular region and straight line, indicating that charge transfer phenomena are more predominant than the mass transfer phenomena.

The equivalent electrical circuit used for fitting the EIS data is also illustrated in **Figure 1D**. In this circuit, impedance to current flow arises from the ohmic resistance of the electrolyte between the reference and working electrodes, called uncompensated resistance (R_s), and denoted as R_1 . The value of R_1 is determined by the distance between the reference and working electrodes for a specific electrolyte. R_1 is placed in series within the circuit. At both very high and very low frequencies, the circuit exhibits resistive behavior, causing the semicircle to shift to the real axis. At very high frequencies, Z_{real} equals R_s , while at low frequencies, Z_{real} equals R_{CT} ($R_1 + R_2$). These boundary conditions are depicted in the Nyquist plot as the first and second intersections of the semicircle with the x-axis. Additionally, this circuit is connected in series with a second parallel circuit. Within this parallel arrangement, Q_3 and Q_4 represent parameters containing capacitance

information. The series connection Q3/R3 signifies gas diffusion coupled with charge transfer reactions and ionic transport within the anode functional layer [13]. Ohmic resistances (R_s), i.e., bulk electrolyte-electrode resistances obtained from the intercepts of the X-axis, were 9.18 Ω , 8.19 Ω , and 7.19 Ω , for RGO, hBN-RGO, and Bph-RGO respectively. Moreover, the R_{CT} values of 38.83 Ω (RGO), 33.48 Ω (hBN-RGO), and 29.22 Ω (Bph-RGO) implied a lower charge transfer resistance between the solid-liquid interface for the 2D-functionalized graphene sponges (**Table S4**).

Dopants improve the charge density and electrostatic capacity of the double layer by promoting the space-charge capacitance [15,16]. The electrostatic capacity of each electrode in the double layer is represented by the C_{dl} [17]. In our previous study [6], the calculated values of C_{dl} were 0.067 F g⁻¹ (RGO), 0.081 F g⁻¹ (hBN-RGO) and 0.90 F g⁻¹ (Bph-RGO). These values reflect the ability of the double layer to store electrical charge in response to an applied potential by effectively saturating the cavities within the open RGO structure. These cavities contain ionic liquid and adsorbed counterions, resulting in the formation of a filled phase and a dilute charged phase [18,19]. This charge storage mechanism allows for the subsequent release of the stored charge during the OFF stage. Higher C_{dl} (e.g., Bph-RGO) implies a higher number of ions that trap in co-ions in the crowded phase (rigid and diffusion-controlled layer), resulting in a slow diffusion out of the cavity into the dilute counterion-rich phase. Thus, functionalization of graphene with the 2D materials enhances: *i*) electrostatic interactions between the electrolyte ions and electrodes; *ii*) charge transfer at the electrode/electrolyte interface and *iii*) ionic binding capability for charging/discharging processes, leading to an enhanced accommodation of ions at the electrode surface [20,21].

3.2 Electrooxidation of persistent organic contaminants

Normalized effluent concentrations of the target contaminants in the initial open circuit (OC_{initial}), during the application of current and in the final open circuit (OC_{final}) for the two evaluated systems are presented in **Figures S1**. In the initial OC, TCP exhibited less than 5% removal at both hBN- and Bph-RGO anode, thus excluding adsorption as a relevant removal mechanism for this contaminant. In the case of IPM, its removal in the OC was 24% for Bph-RGO anode, and 13% for hBN-RGO anode, respectively. Given the high polarity of IPM ($\log D = -2.1$, **Table S5**), its removal in the OC can be explained by an enhanced electrostatic adsorption onto the graphene sponge electrode surface due to its higher polar surface area (169 \AA^2) (**Table S5**). CBZ exhibited the highest removal in the initial OC, with 25 and 48% removal at the Bph-RGO and hBN-RGO anode, respectively (**Figure S1 E-F**). CBZ has the highest $\log D$ value among the investigated contaminants ($\log D = 2.3$, **Table S5**), and has a high tendency for π - π interactions with the electrode surface due to the abundant double bonds and aromatic rings in its structure. Enhanced adsorption of CBZ at the hBN-RGO anode can be explained by the enhanced π - π stacking between the aromatic rings of CBZ and the hexagonal cells of hBN [6].

Functionalized graphene sponges showed an enhanced generation of oxidant species in all cycles of intermittent current tested compared to the undoped RGO. In both functionalized anodes tested, 52.5s ON/OFF and 75s/30s ON/OFF cycles yielded the highest levels for oxidant generation. For instance, the cycles of 52.5s ON/OFF and 75s/30s ON/OFF yielded similar concentration of oxidants to the ones generated with continuous current application, e.g., 31-36 μM of H_2O_2 and 1.2×10^{-7} - 2.5×10^{-7} μM of $\cdot\text{OH}$ (**Figure 2 A-B**). The lower concentration of the measured oxidant species in 105 s/105 s cycles confirms the capacitive properties of the graphene sponge electrodes,

where charge is retained for short periods of time and dissipates more during longer OFF stages. The application of intermittent current resulted in higher concentrations of ozone measured for the hBN-RGO anode (Figure 2 C).

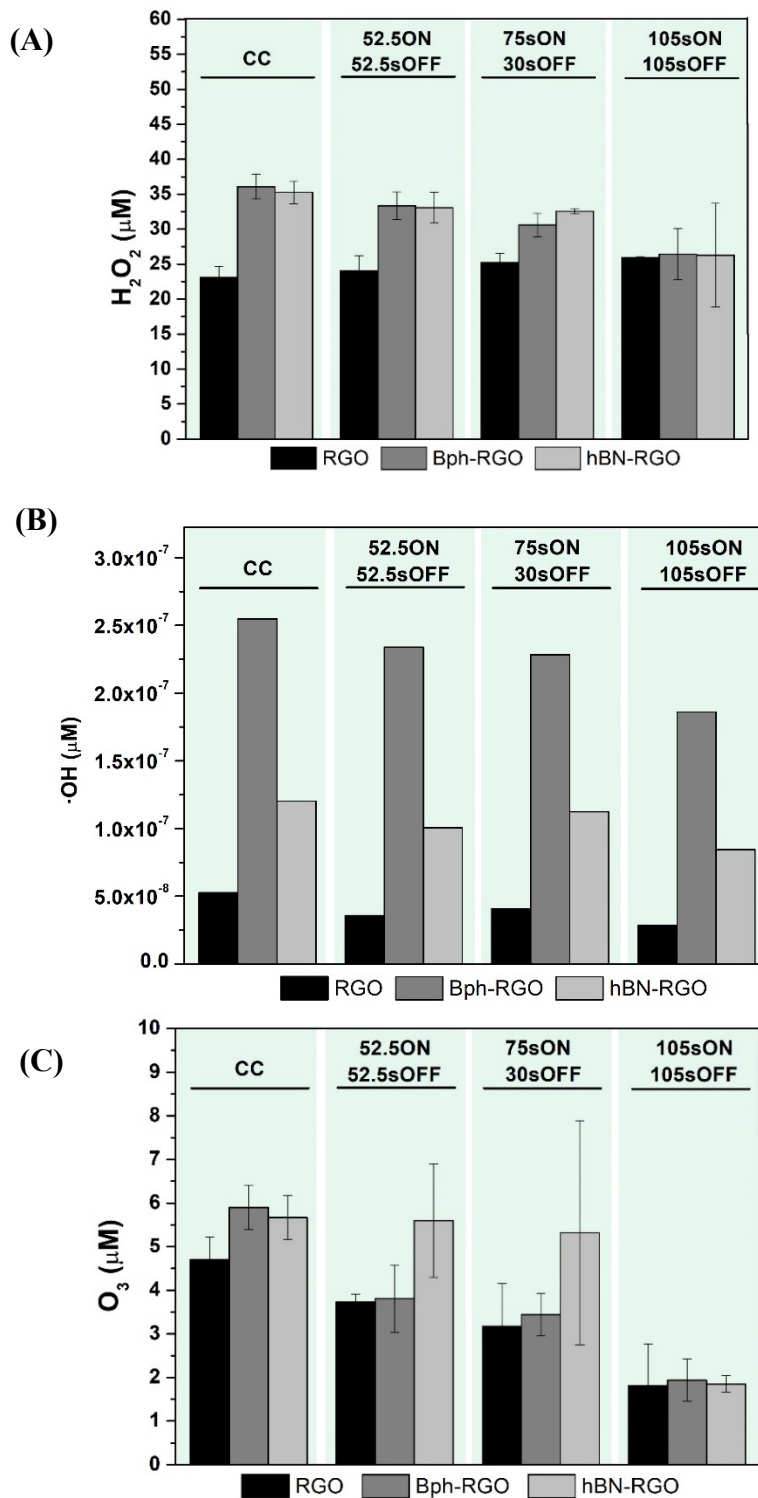


Figure 2. Measured concentrations of oxidants at 231 A m^{-2} using RGO, Bph-RGO and hBN-RGO anode, each coupled to N-RGO cathode: **A)** H_2O_2 , **B)** $\cdot\text{OH}$ radicals, and **B)** ozone.

Electrochemical experiments were conducted by applying a continuous current density of 231 Am^{-2} to RGO, Bph-RGO and hBN-RGO anode. This yielded an ohmic-drop corrected anode potential ranging from 3.1 to 4.5 V/SHE, with a recorded anode potential between 6- 8.2 V/SHE. However, in the case of three intermittent current cycles, the ohmic-drop corrected anode potential ranged from 5.1 - 6.1 V/SHE, while the recorded anode potential ranged from 7.9 - 9.1 V/SHE (**Table S7**). The observed increase in the anode potentials during intermittent current experiments conducted on all tested anodes can be attributed to capacitance and ion diffusion during charge and discharge processes within the graphene sponge electrodes. It is noteworthy that aqueous electrolytes with lower ionic conductivity (1 mS cm^{-1}) exhibit reduced rates of ion mobility and electrode charging/discharging [2,22]. Consequently, the restricted diffusion of ions within the low-conductivity electrolyte, combined with increased ohmic losses, results in elevated electrode potentials [23]. Therefore, during intermittent current application, graphene sponge electrodes retain the charge more during the shorter OFF stages, to yield a higher total cell potential compared to continuous current. The increase in the ohmic-drop corrected anode in intermittent current mode is more pronounced for the Bph-RGO anode compared to the hBN-RGO anode, given that higher C_{dl} of Bph-RGO, as discussed in section 3.1, leads to its slower discharge.

Figure 3 shows the removal percentages of the target contaminants at 231 A m^{-2} of anodic current density using RGO, Bph-RGO and hBN-RGO anode, respectively, in continuous current mode and in three different intermittent current modes. Switching from continuous to intermittent current led to a significant decrease in the removal efficiencies of CBZ when using the undoped-RGO anode, i.e., from 50% to 28-35%, respectively. Nevertheless, in the case of functionalized graphene sponge electrodes, CBZ removal was much less affected by introducing the OFF cycles, with a

more notable decrease in the removal efficiency observed in the 105/105 cycle (i.e., 53-56% removal) with longer OFF stage. In contrast, employing short symmetric pulses of 52.5 /52.5 ON/OFF demonstrated comparable CBZ removal efficiency to that achieved through continuous current. (Figure 3A).

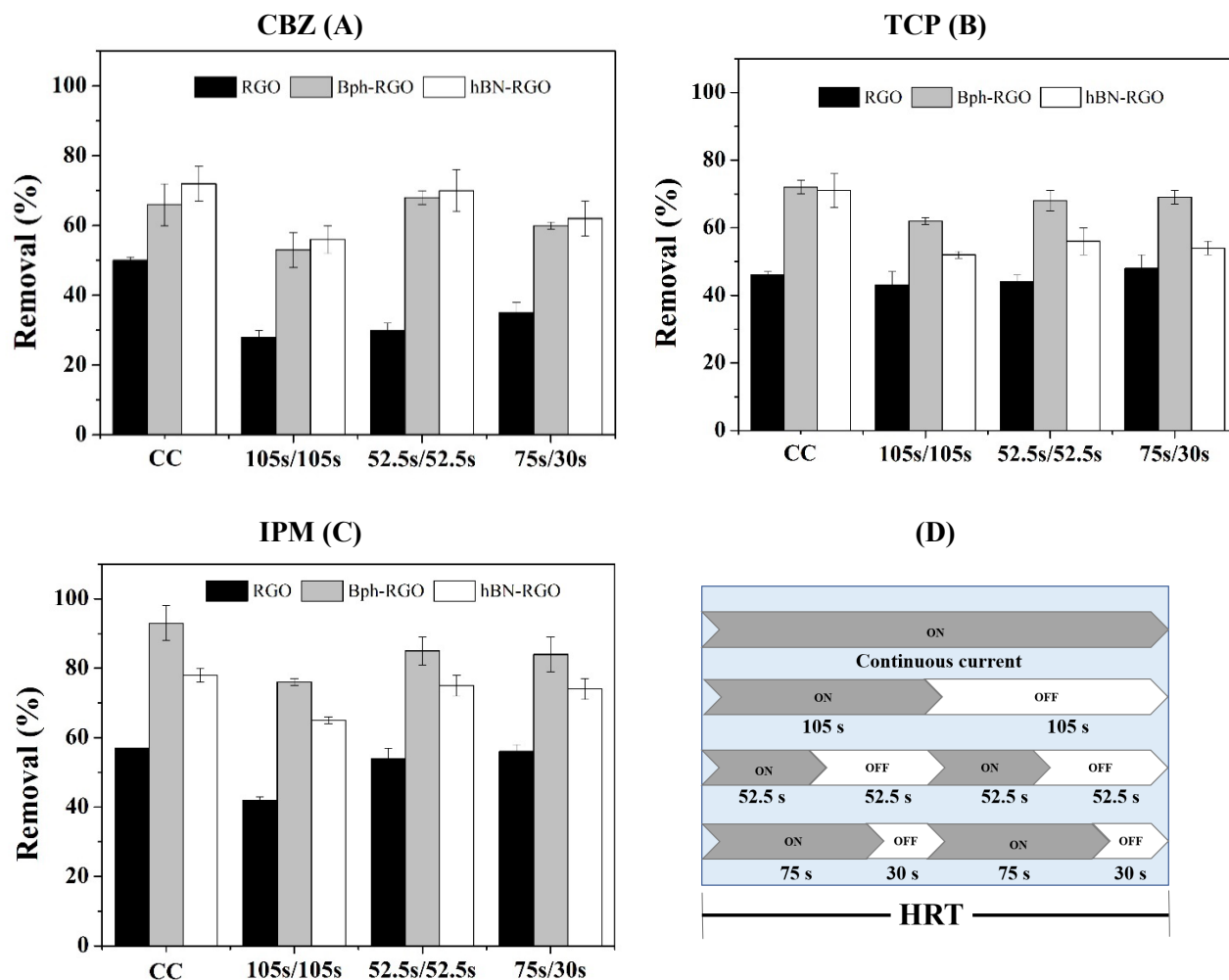


Figure 3. Electrochemical removal of **A)** CBZ, **B)** TCP, and **C)** IPM using undoped RGO, Bph-RGO and hBN-RGO anodes each coupled to N-RGO cathode, at 231 A m^{-2} in the continuous and intermittent current mode. **D)** Graphic representation of the direct current and the different variations of applied intermittent current.

The removal of TCP at the non-functionalized RGO anode was 43-48% and it was minimally affected by the application of intermittent current, likely due to the stronger electrostatic

interactions of the negatively charged TCP with the positively charged graphene sponge anode, as well as π - π interactions of the TCP molecule and the RGO (**Figure 3B**). Similar results were obtained for the Bph-RGO anode, with 62-72% removal with both continuous and intermittent current. In the case of hBN-RGO anode, application of intermittent current decreased the removal of TCP from 71% with continuous current to 52-56% with intermittent current.

Application of an intermittent current with short OFF periods (e.g., 52.5s/52.5s and 75s/30s ON/OFF) did not have a significant impact on the removal of IPM compared to the continuous current application, yielding 74-85% IPM removal when using hBN and Bph-RGO anodes (**Figure 3C**). Electrochemical degradation of IPM can occur through direct electron transfer to the anode as well as through the generation of electrochemical oxidants (e.g., O_3 and $\cdot OH$); IPM is persistent towards O_3 , whereas it is more reactive with $\cdot OH$, with the bimolecular rate constants of $3.34 \times 10^9 \text{ M}^{-1} \text{ s}^{-1}$ (**Table S6**). Thus, its electrochemical degradation proceeds via direct electrolysis and/or electrogenerated $\cdot OH$ and thus is strongly impacted by their interaction with the functionalized-anodes surface.

On the other hand, in a continuous flow mode, where the mix of contaminants is continuously fed into the reactor and removed, the rate of change of concentration ($d[\text{contaminant}]/dt$) can be expressed as the difference between the inlet concentration ($[A]_0$) and the outlet concentration ($[A]$) divided by hydraulic residence time (τ) of 3.45 min of target contaminants in the reactor. According to the results (**Table S8**), the kinetic constants for contaminant removal ranged from 0.08 - 0.16 min^{-1} (for the RGO anode) to 0.15 - 0.27 min^{-1} when using anodes functionalized with 2D materials, under both continuous and intermittent current conditions.

In summary, functionalization of the graphene sponge anode with hBN and Bph led to a significant improvement in the removal of all target contaminants, as well as their respective kinetic constants

in both continuous and intermittent current application modes. This can be explained by the favored interactions of contaminants with the anode surface, such as promoted π - π interactions of CBZ with the hBN-RGO anode, and enhanced generation of oxidant species at the Bph-RGO anode (**Figure 2**). The removal efficiencies of the target contaminants were better maintained at the Bph-RGO anode when switching to an intermittent current application, in accordance with its higher C_{dl} . (0.090 F g^{-1}) compared with the hBN-RGO (0.081 F g^{-1}). The use of intermittent current facilitates the evacuation of oxygen bubbles formed at the anodes during the OFF cycles and enhances the interaction of the target contaminants with the electrode surface. The use of a symmetric cycle with short ON and OFF periods (e.g., 52.5s/52.5s ON/OFF) was the most effective strategy for the removal of target contaminants. In this case, Bph-RGO anode showed predominance in the elimination of IPM and TCP, undergoing electrostatic interactions and reactions with the electrogenerated $\cdot\text{OH}$. CBZ interacts better with the hBN-RGO anode via Van der Waals forces, in addition to π - π interactions. Even though the large electronegativity difference between boron and oxygen ($\delta \sim 1.4$) results in a polarized and hydrophilic surface [24] of the Bph-RGO anode, the dielectric properties of hBN-RGO facilitate the interaction of the anode with pollutant molecules during ON/OFF cycles. The final OC did not show an increase in the effluent concentrations compared to the initial OC (**Figure S1**), implying the electrochemical degradation of the target contaminants in both continuous and intermittent current mode, as opposed to electrosorption only.

The electrochemical removal of a set of contaminants using 2D-functionalized sponges with the intermittent current mode resulted in significant energy savings, reducing the energy consumption from 27.1 kWh m^{-3} (RGO) to 24 kWh m^{-3} in continuous current mode for both Bph-RGO and hBN-RGO anodes at 231 A m^{-2} to $11\text{-}13 \text{ kWh m}^{-3}$ (52.5s and 105s ON/OFF cycles), $15\text{-}18 \text{ kWh}$

m^{-3} (75s ON/30s OFF) for hBN-RGO and Bph-RGO, respectively (**Table S9**). Hence, employing symmetric intermittent current modes with short ON/OFF cycles may provide notable energy savings while maintaining the efficiency in the degradation of persistent organic contaminants.

On the other hand, the high energy consumption observed is caused by the choice of the phosphate buffer as the supporting electrolyte, as slow diffusion of phosphate ions within the graphene sponge electrode, caused by their higher hydration energy and larger size, increases the R_{CT} of the material [25]. More realistic streams with lower amount of phosphate lead to a much lower potential drop through the graphene sponge electrodes and thus lower energy consumption, as explained in section 3.4 on the example of secondary treated municipal wastewater effluent.

Table S10 shows studies where a commercial anode material, BDD, was utilized for oxidizing CBZ, IPM and TCP. RGO-based sponges showed removal rates like those achieved by BDD, with consistent oxidation rate, and lower energy consumption. RGO-based electrodes often required half the energy used in contaminant oxidation with BDD. Many previous studies used unrealistic conditions, such as high-conductivity electrolytes and unrealistic contaminant concentrations, without testing in real water streams. In contrast, this study filled this crucial gap by testing in real-world conditions, making our approach highly practical and widely applicable.

3.3 Elucidation of the transformation products of carbamazepine

To gain insight into the electrochemical degradation pathways of organic pollutants using Bph-RGO and hBN-RGO anode, high resolution mass spectrometry was employed to elucidate the degradation pathways of CBZ as a model contaminant. **Figure S2 -S7** show the mass spectra and **Table S11** summarizes the retention times, experimental m/z and exact mass measurement error values of the identified TPs. The identified TPs imply that the degradation of CBZ occurs through

oxidation and reduction reactions at both Bph-RGO and hBN-RGO systems (**Figure 4 and 5**). The electrochemical degradation of CBZ involves amide hydrolysis, where the carbonyl oxygen undergoes protonation and reacts with water, resulting in the formation of the corresponding carboxylic acid and CBZ-193 [26]. This reaction occurs at both Bph- and hBN-RGO anodes. Additionally, the formation of CBZ-250 [27], which is attributed to hydroxylation and ring contraction [27,28] (**Figure S8**), was observed using both 2D-functionalized anodes. The interaction between CBZ and the electron-deficient boron atoms in hBN and Bph-RGO (acting as Lewis acids) can lead to the formation of new bonds between the nonbonding electrons of CBZ and boron from the sponges. This interaction is likely responsible for hydrolysis, hydroxylation, and ring contraction reaction of CBZ.

Due to its poor reactivity with ozone (**Table S6**), CBZ molecule often reacts with $\cdot\text{OH}$ at the olefinic double bond (C10-C11) on the central heterocyclic ring. This reaction yields an epoxy-intermediate (CBZ-252) [27–29]. The presence of this TP may be attributed to the higher amount of $\cdot\text{OH}$ generated at the Bph-RGO anode compared to the hBN-RGO anode. However, it is important to note that epoxy-intermediate can also be formed by an initial electron transfer from CBZ to the anode [27]. Furthermore, CBZ-256 was identified when using Bph-RGO anode, and assigned to the catalytic hydrogenation of carbonyl and epoxy group from CBZ-252 [30].

The electrochemical reduction of CBZ may be explained by the planar conjugated π electron systems of CBZ, in which electrons are shared and reactions to various double bonds in the molecule are likely to occur. For instance, in the hBN-RGO/N-RGO system, the formation of CBZ-238 can be attributed to the hydrogenation of the double bond [30], followed by the loss of ammonia moiety and hydrogenation to yield CBZ-225. Upon the adsorption of CBZ at the hBN-RGO anode surface, the unsaturated bond of CBZ is activated, enabling its interaction with H^+

ions present at the electrode-electrolyte interface. Consequently, hydrogen is added across the bond, leading to the formation of more saturated TPs.

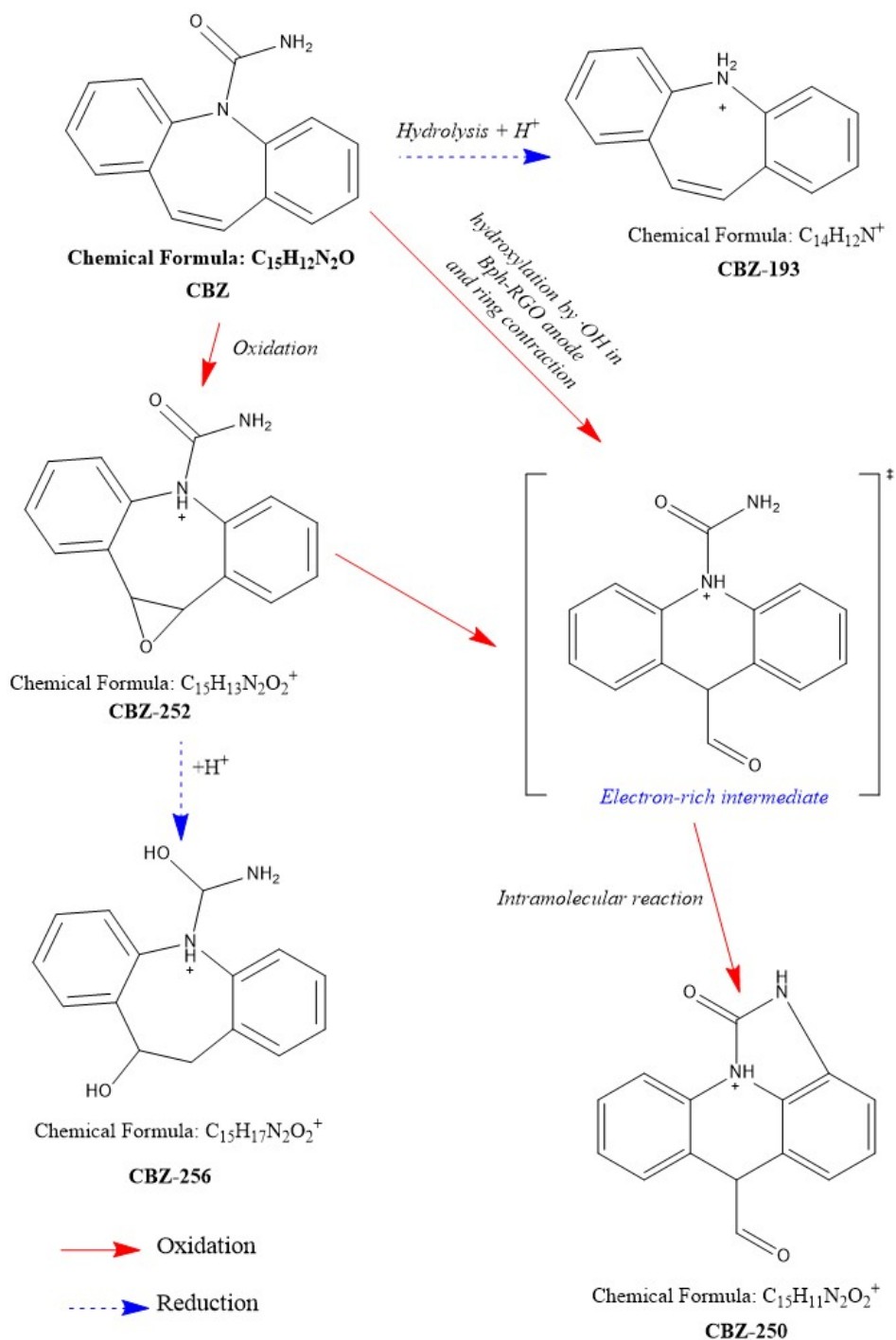


Figure 4. Proposal pathway of electrochemical removal of CBZ using Bph-RGO anode coupled to N-RGO cathode.

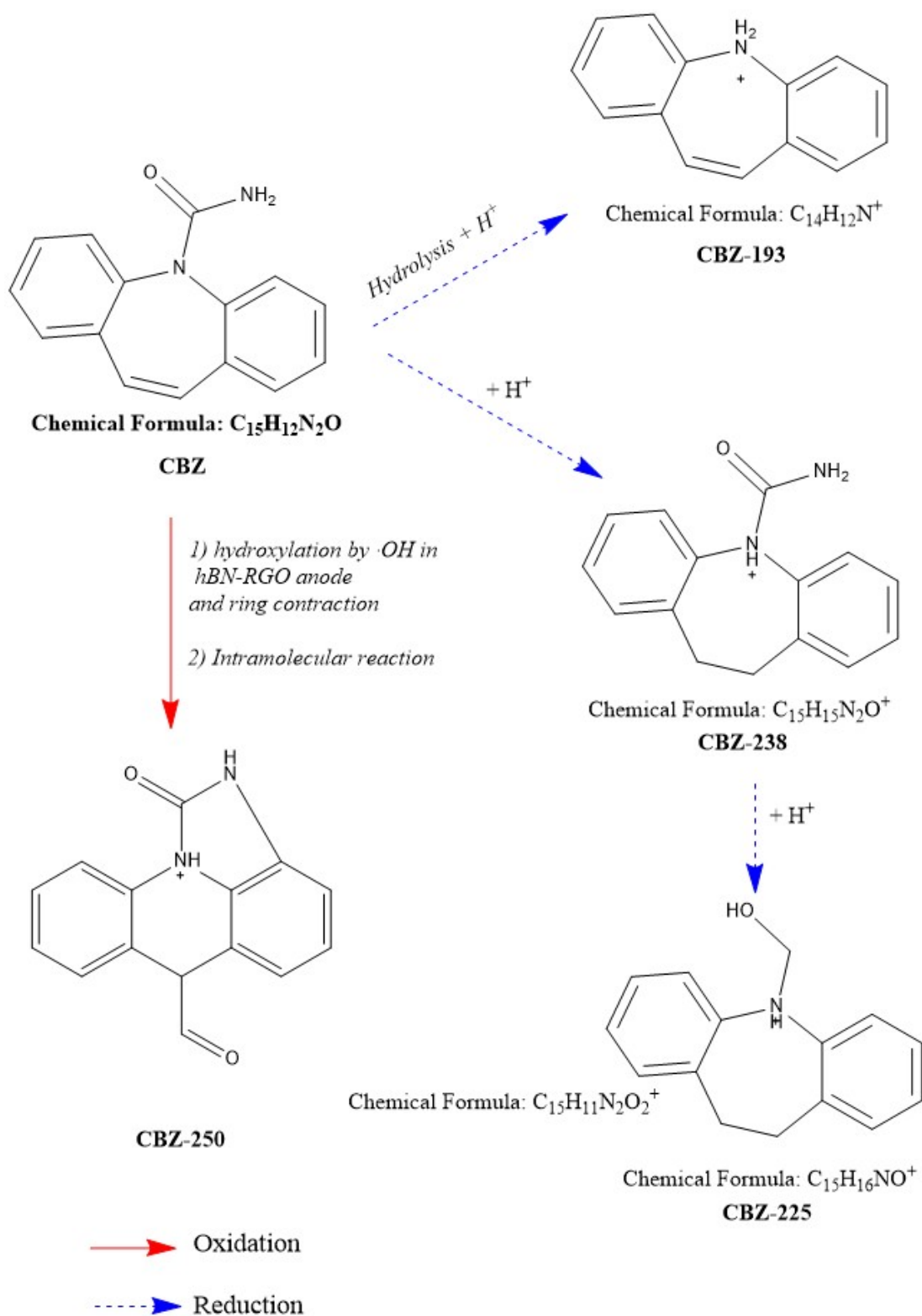


Figure 5. Proposal pathway of electrochemical removal of CBZ using hBN-RGO anode coupled to N-RGO cathode.

Figure S9 illustrates the qualitative profiles of the identified TPs (i.e., peak surface areas of TPs normalized to the initial peak surface area of CBZ). CBZ-193 and CBZ-250, which were observed with both Bph-RGO and hBN-RGO anodes, are more prominently generated when using the hBN-RGO anode. Nevertheless, these TPs exhibited a decrease in their intensity relative to the longer operation times when hBN-RGO was used. For example, CBZ-250 undergoes complete degradation within 30 bed volumes when hBN-RGO is employed, while it remains present in the treated solution with the Bph-RGO anode. The persistent presence of CBZ-193 and CBZ-250 in the Bph-RGO system suggests that CBZ is transformed into these TPs rather than being electrosorbed. On the other hand, in the case of hBN-RGO anode with an enhanced π - π interactions, these TPs are likely more adsorbed onto the sponge. This is supported by the unique identification of CBZ-193 and CBZ-238 in the final OC using hBN-RGO anode. CBZ-256, CBZ-252 and CBZ-225 were identified in lower intensity in relation to the parent compound.

3.4 Experiments with secondary wastewater effluent

Figure 6 illustrates the removal percentages of the target compounds using secondary treated municipal wastewater effluent having the same conductivity as the employed 10 mM phosphate buffer (1.2 mS cm⁻¹, pH 7). The experiments were conducted with Bph-RGO and hBN-RGO anodes, and the effluent was amended with 1 μ M of the target compounds in both continuous and intermittent (52.5s/52.5s ON/OFF) current modes. To address the issue of excessive foaming, which hindered proper reactor operation, the experiment was conducted using a lower current density of 115 A m⁻². This current density was chosen as half the value typically used in the experiments with phosphate buffer.

Switching from continuous to intermittent current led to a decrease in the removal efficiencies for all target contaminants for both hBN-RGO and Bph-RGO anodes. Nevertheless, the decline

observed in both continuous and intermittent current modes was less than 30% when compared to the experiments conducted in phosphate buffer at 231 A m^{-2} . For instance, the removal of CBZ decreased from 56-63% with continuous current to 45-52% with intermittent current for hBN-RGO and Bph-RGO anode, respectively. The removal efficiency of TCP at the Bph-RGO and hBN-RGO anodes exhibited a comparable impact when employing 52.5s/52.5s ON/OFF cycles, the efficiency decreased from 60% with the continuous current to 43% with the intermittent current. The removal of IPM was slightly more affected by switching to an intermittent current for the Bph-RGO anode, with percentages ranging from 58-78%, compared to 56-66% for the hBN-RGO anode. This difference can possibly be attributed to the scavenging of $\cdot\text{OH}$ produced at the Bph-RGO anode by the organic matter.

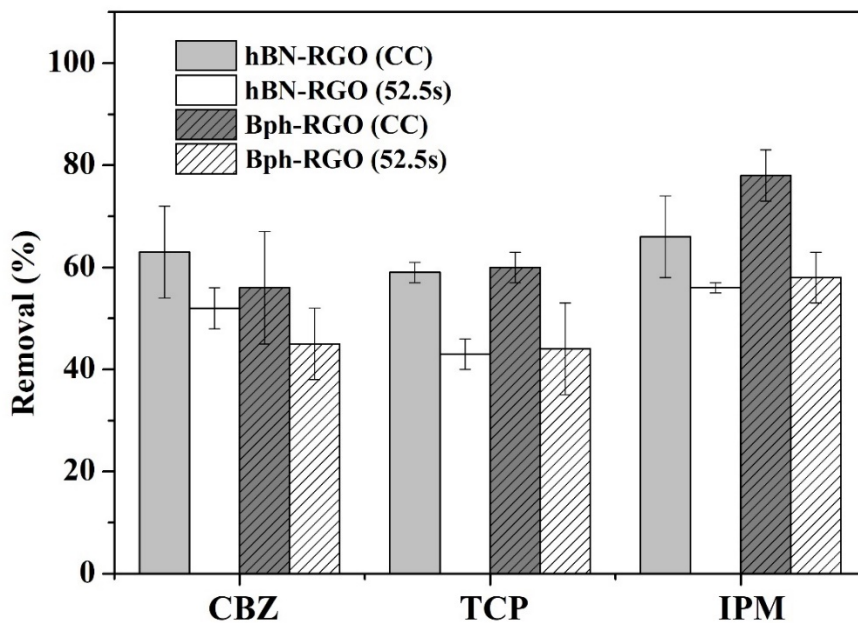


Figure 6. Electrochemical removal of target contaminants in secondary wastewater effluent using Bph-RGO and hBN-RGO anodes each coupled to N-RGO cathode, at 115 A m^{-2} in intermittent current mode 52.5s ON / 52.5s OFF.

The use of real wastewater effluent as a supporting electrolyte with the Bph and hBN-RGO anodes demonstrated an enhancement in the removal efficiency of target contaminants relative to the applied current density. This enhancement can be ascribed to the influence of the various ions present in the wastewater effluent (**Table S1**), which positively impacted the performance of the functionalized anodes. For instance, ions like Na^+ and Cl^- (158 and 210 mg L^{-1}) yield a weaker solvation shell [31], which gives them a higher degree of mobility in the pores of electrode surface, leading to a more uniform charge distribution [32,33] and charge density of the double layer [34]. In contrast, phosphate exhibits a stronger solvation shell [31], indicating a tightly bound arrangement of water molecules around it, resulting in a highly structured and cohesive solvation shell. This compact solvation structure makes it more challenging for phosphate buffer ions to adsorb onto the electrode surface, thus affecting ionic transport between the electrode and electrolyte and consequently the efficiency of contaminant removal. The impact of the electrolyte anions on the graphene sponge performance and resistance (i.e., R_{CT} , $\text{PB} > \text{NaNO}_3 > \text{NaCl}$) was also demonstrated by the electrochemical impedance spectroscopy (EIS) measurements conducted in our recent study [25]. In **Figure S10**, the Nyquist plot shows a significantly lower R_{CT} of approximately 14 Ω when using wastewater as the electrolyte compared to 33.48 Ω and 29.22 Ω for hBN-RGO and Bph-RGO, respectively, when using phosphate buffer. This difference is attributed to the easier insertion of ions, such as Cl^- and SO_4^{2-} , which are predominantly found in the secondary treated wastewater effluent, between the layers of reduced graphene oxide (RGO) in the graphene sponge anode coating, as opposed to the larger phosphate ions [25].

The use of secondary wastewater minimized ohmic losses with Bph and hBN-RGO anodes by improving the contact between the electrodes and electrolyte, thus maximizing the energy efficiency and the overall performance of the system. The energy consumption was reduced from

9.3 to 4.4 kWh m⁻³ (Bph-RGO anode), and from 6.9 to 3.6 kWh m⁻³ (hBN-RGO anode) applying direct and intermittent current (52.5s/52.5s ON/OFF), respectively (**Table S8**). The use of secondary effluent resulted in a significant reduction in energy consumption and an improvement in the contaminant removal efficiency compared to phosphate buffer. Given that the electrical conductivity of the secondary effluent was the same as for the employed 10 mM phosphate buffer (~1 mS cm⁻¹), this reduced resistance of the graphene sponge electrodes highlights the impact of supporting electrolyte composition on the electrochemical behavior of the RGO-based material [25].

Conclusions

Functionalizing graphene sponge anodes with 2D materials improves their capacitive properties and enhances the electrostatic interactions between ions and electrode surface, charge transfer, and ionic binding capability. Switching from continuous current to intermittent current with shorter OFF stages (i.e., 52.5s and 75s/30s ON/OFF) reveals similar outcomes in terms of oxidant species generation and organic contaminant removal compared to the continuous current mode. This can be attributed to the double layer capacitance of the graphene sponges functionalized with 2D materials, enabling improved contact between the contaminants and the oxidizing species on the electrode surface, as well as efficient removal of the oxygen and hydrogen bubbles generated in the reactor. This strategy reduces the energy consumption from 24 kWh m⁻³ in direct current mode for both Bph-RGO and hBN-RGO anodes to 11-13 kWh m⁻³ (52.5s ON/OFF cycles).

A total of six TPs of CBZ were detected with both functionalized anodes, formed by both oxidation and reduction reactions. Notably, TPs like CBZ-193 and CBZ-250 are predominant in both systems, making it difficult to clearly elucidate the differences in their interactions with Bph and

hBN-RGO anode. However, there is a discernible trend indicating the adsorption of certain TPs onto the hBN sponge.

The removal efficiency of target contaminants using wastewater in both continuous and intermittent current modes (52.5s/52.5s ON-OFF) at 115 A m^{-2} was 56-78% and 43-58%, respectively. The electrochemical systems with hBN and Bph-RGO anodes could remove ~60 % of the TCP and IPM from municipal wastewater, whereas the removal of CBZ was somewhat higher for the hBN-RGO anode (63%) compared with the Bph-RGO anode (56%) due to the enhanced π - π interactions in the first case. The scavenging effect of organic matter on $\cdot\text{OH}$ production has a greater impact on the removal of the most hydrophilic compounds, such as IPM and TCP, leading to lower degradation when using intermittent current compared with the continuous current. The application of an intermittent mode (52.5s/52.5s ON-OFF) resulted in a significant reduction in energy consumption from 9.3 kWh m^{-3} to 4.4 kWh m^{-3} using Bph-RGO and from 6.9 kWh m^{-3} to 3.6 kWh m^{-3} using hBN-RGO. This study demonstrates the potential of using 2D-functionalized graphene sponge electrodes in the intermittent current mode, thus exploiting the capacitive properties of graphene, and enabling energy savings.

Acknowledgement

The authors acknowledge ERC Starting Grant project ELECTRON4WATER (Three-dimensional nanoelectrochemical systems based on low-cost reduced graphene oxide: the next generation of water treatment systems), project number 714177. The authors acknowledge the support from the Economy and Knowledge Department of the Catalan Government through a Consolidated Research Group (ICRA-TECH - 2021 SGR 01283) and funding from CERCA program.

References

- [1] C. Hu, Y. Lin, J.W. Connell, H. Cheng, Y. Gogotsi, M. Titirici, L. Dai, Carbon-based metal-free catalysts for energy storage and environmental remediation, *Adv. Mater.* 31 (2019) 1806128. <https://doi.org/10.1002/adma.201806128>.
- [2] G.-F. Norra, L. Baptista-Pires, E. Cuervo Lumbaque, C. M. Borrego, J. Radjenovic, Chlorine-free electrochemical disinfection using graphene sponge electrodes, *Chem. Eng. J.* 430 (2021) 132772. <https://doi.org/10.1016/j.cej.2021.132772>.
- [3] L. Baptista-Pires, G.-F. Norra, J. Radjenovic, Graphene-based sponges for electrochemical degradation of persistent organic contaminants, *Water Res.* 203 (2021) 117492. <https://doi.org/10.1016/j.watres.2021.117492>.
- [4] N. Ormeno-Cano, J. Radjenovic, Electrochemical degradation of antibiotics using flow-through graphene sponge electrodes, *J. Hazard. Mater.* 431 (2022) 128462.
- [5] A.J.P. Neto, E.E. Fileti, Differential capacitance and energetics of the electrical double layer of graphene oxide supercapacitors: Impact of the oxidation degree, *J. Phys. Chem. C.* 122 (2018) 21824–21832. <https://doi.org/10.1021/acs.jpcc.8b07349>.
- [6] E.C. Lumbaque, L. Baptista-Pires, J. Radjenovic, Functionalization of graphene sponge electrodes with two-dimensional materials for tailored electrocatalytic activity towards specific contaminants of emerging concern, *Chem. Eng. J.* (2022) 137057. <https://doi.org/10.1016/j.cej.2022.137057>.
- [7] F. Barzegar, A. Bello, O. Guellati, D.Y. Momodu, A. Harat, J.K. Dangbegnon, M. Guerioune, N. Manyala, Effect of addition of different carbon materials on hydrogel derived carbon material for high performance electrochemical capacitors, *Electrochim. Acta.* 186 (2015) 277–284. <https://doi.org/10.1016/j.electacta.2015.10.189>.
- [8] A.N. Baga, G.R.A. Johnson, N.B. Nazhat, R.A. Saadalla-Nazhat, A simple spectrophotometric determination of hydrogen peroxide at low concentrations in aqueous solution, *Anal. Chim. Acta.* 204 (1988) 349–353. [https://doi.org/10.1016/S0003-2670\(00\)86374-6](https://doi.org/10.1016/S0003-2670(00)86374-6).
- [9] S. Nayak, B.P. Chaplin, Fabrication and characterization of porous, conductive, monolithic Ti₄O₇ electrodes, *Electrochim. Acta.* 263 (2018) 299–310. <https://doi.org/10.1016/j.electacta.2018.01.034>.
- [10] Z. Lei, L. Lu, X.S. Zhao, The electrocapacitive properties of graphene oxide reduced by urea, *Energy Environ. Sci.* 5 (2012) 6391–6399. <https://doi.org/10.1039/C1EE02478G>.
- [11] N. Elgrishi, K.J. Rountree, B.D. McCarthy, E.S. Rountree, T.T. Eisenhart, J.L. Dempsey, A practical beginner's guide to cyclic voltammetry, *J. Chem. Educ.* 95 (2018) 197–206. <https://doi.org/10.1021/acs.jchemed.7b00361>.
- [12] Y. Abdi, A. Mazaheri, S. Hajibaba, S. Darbari, S.J. Rezvani, A. Di Cicco, F. Paporoni, R. Rahighi, S. Gholipour, A. Rashidi, A two-dimensional borophene supercapacitor, *ACS Mater. Lett.* 4 (2022) 1929–1936. <https://doi.org/10.1021/acsmaterialslett.2c00475>.
- [13] A.C. Lazanas, M.I. Prodromidis, Electrochemical Impedance Spectroscopy— A Tutorial, *ACS Meas. Sci. Au.* (2022). <https://doi.org/10.1021/acsmesuresciau.2c00070>.
- [14] V. Vivier, M.E. Orazem, Impedance analysis of electrochemical systems, *Chem. Rev.* 122 (2022) 11131–11168. <https://doi.org/10.1021/acs.chemrev.1c00876>.
- [15] D. Tashima, K. Kurosawatsu, M. Uota, T. Karashima, Y.M. Sung, M. Otsubo, C. Honda, Space charge behaviors of electric double layer capacitors with nanocomposite electrode, *Surf. Coatings Technol.* 201 (2007) 5392–5395.

- <https://doi.org/10.1016/j.surfcoat.2006.07.045>.
- [16] K. Liu, C. Yu, Y. Xie, W. Guo, J. Yu, L. Ni, Z. Wang, R. Fu, J. Qiu, Correlation between self-discharge behavior and heteroatoms over doped carbon sheets for enhanced pseudocapacitance, *J. Energy Chem.* 72 (2022) 291–298. <https://doi.org/10.1016/j.jechem.2022.05.004>.
- [17] J.N. Neal, D.J. Wesolowski, D. Henderson, J. Wu, Electric double layer capacitance for ionic liquids in nanoporous electrodes: Effects of pore size and ion composition, *J. Mol. Liq.* 270 (2018) 145–150.
- [18] K. Breitsprecher, C. Holm, S. Kondrat, Charge me slowly, I am in a hurry: Optimizing charge–discharge cycles in nanoporous supercapacitors, *ACS Nano.* 12 (2018) 9733–9741.
- [19] D. Boonpakdee, C.F.G. Yévenes, W. Surareungchai, Exploring non-linearities of carbon-based microsupercapacitors from an equivalent circuit perspective, *J. Mater. Chem. A.* 6 (2018) 7162–7167. <https://doi.org/10.1039/C8TA01995A>.
- [20] H.M. Jeong, J.W. Lee, W.H. Shin, Y.J. Choi, H.J. Shin, J.K. Kang, J.W. Choi, Nitrogen-doped graphene for high-performance ultracapacitors and the importance of nitrogen-doped sites at basal planes, *Nano Lett.* 11 (2011) 2472–2477. <https://doi.org/10.1021/nl2009058>.
- [21] H.R. Jiang, Z. Lu, M.C. Wu, F. Ciucci, T.S. Zhao, Borophene: a promising anode material offering high specific capacity and high rate capability for lithium-ion batteries, *Nano Energy.* 23 (2016) 97–104. <https://doi.org/10.1016/j.nanoen.2016.03.013>.
- [22] J. Zhu, Y. Xu, J. Wang, J. Lin, X. Sun, S. Mao, The effect of various electrolyte cations on electrochemical performance of polypyrrole/RGO based supercapacitors, *Phys. Chem. Chem. Phys.* 17 (2015) 28666–28673. <https://doi.org/10.1039/C5CP04080A>.
- [23] B.E. Logan, E. Zikmund, W. Yang, R. Rossi, K.-Y. Kim, P.E. Saikaly, F. Zhang, Impact of ohmic resistance on measured electrode potentials and maximum power production in microbial fuel cells, *Environ. Sci. Technol.* 52 (2018) 8977–8985. <https://doi.org/10.1021/acs.est.8b02055>.
- [24] A. Joshi, A.K. Tomar, G. Singh, R.K. Sharma, Engineering oxygen defects in the boron nanosheet for stabilizing complex bonding structure: An approach for high-performance supercapacitor, *Chem. Eng. J.* 407 (2021) 127122. <https://doi.org/10.1016/j.cej.2020.127122>.
- [25] N. Duinslaeger, A. Doni, J. Radjenovic, Impact of supporting electrolyte on electrochemical performance of borophene-functionalized graphene sponge anode and degradation of per- and polyfluoroalkyl substances (PFAS), *Water Res.* 242 (2023) 120232. <https://doi.org/10.1016/j.watres.2023.120232>.
- [26] M. Samara, A. Nasser, U. Mingelgrin, Mechanochemical removal of carbamazepine, *Chemosphere.* 160 (2016) 266–272. <https://doi.org/10.1016/j.chemosphere.2016.06.082>.
- [27] M.M. Ahmed, S. Chiron, Solar photo-Fenton like using persulphate for carbamazepine removal from domestic wastewater, *Water Res.* 48 (2014) 229–236. <https://doi.org/10.1016/j.watres.2013.09.033>.
- [28] A. Jelic, I. Michael, A. Achilleos, E. Hapeshi, D. Lambropoulou, S. Perez, M. Petrovic, D. Fatta-Kassinos, D. Barcelo, Transformation products and reaction pathways of carbamazepine during photocatalytic and sonophotocatalytic treatment, *J. Hazard. Mater.* 263 (2013) 177–186. <https://doi.org/10.1016/j.jhazmat.2013.07.068>.
- [29] T. Kosjek, H.R. Andersen, B. Kompore, A. Ledin, E. Heath, Fate of carbamazepine during water treatment, *Environ. Sci. Technol.* 43 (2009) 6256–6261. <https://doi.org/10.1021/es900070h>.

- [30] A. König, C. Weidauer, B. Seiwert, T. Reemtsma, T. Unger, M. Jekel, Reductive transformation of carbamazepine by abiotic and biotic processes, *Water Res.* 101 (2016) 272–280. <https://doi.org/10.1016/j.watres.2016.05.084>.
- [31] K.D. Collins, Charge density-dependent strength of hydration and biological structure, *Biophys. J.* 72 (1997) 65–76. [https://doi.org/10.1016/S0006-3495\(97\)78647-8](https://doi.org/10.1016/S0006-3495(97)78647-8).
- [32] C. Merlet, M. Salanne, B. Rotenberg, P.A. Madden, Influence of solvation on the structural and capacitive properties of electrical double layer capacitors, *Electrochim. Acta.* 101 (2013) 262–271. <https://doi.org/10.1016/j.electacta.2012.12.107>.
- [33] C. Zhan, M.R. Cerón, S.A. Hawks, M. Otani, B.C. Wood, T.A. Pham, M. Stadermann, P.G. Campbell, Specific ion effects at graphitic interfaces, *Nat. Commun.* 10 (2019) 4858. <https://doi.org/10.1038/s41467-019-12854-7>.
- [34] A.R. Finney, I.J. McPherson, P.R. Unwin, M. Salvalaglio, Electrochemistry, ion adsorption and dynamics in the double layer: a study of NaCl (aq) on graphite, *Chem. Sci.* 12 (2021) 11166–11180. <https://doi.org/10.1039/d1sc02289j>.

Supplementary Material

Electro-oxidation of persistent organic contaminants at graphene sponge electrodes using intermittent current

Elisabeth Cuervo Lumbaque ^{a,b}, Jelena Radjenovic^{a,c}

^a*Catalan Institute for Water Research (ICRA), Emili Grahit 101, 17003 Girona, Spain*

^b*University of Girona, Girona, Spain*

^c*Catalan Institution for Research and Advanced Studies (ICREA), Passeig Lluís Companys 23,
08010 Barcelona, Spain*

* *Corresponding author:*

Jelena Radjenovic, Catalan Institute for Water Research (ICRA), Emili Grahit 101, 17003 Girona, Spain

Phone: + 34 972 18 33 80; Fax: +34 972 18 32 48; E-mail: jradjenovic@icra.cat

Text S1. Analytical methods

Target organic contaminants were analyzed with a 5500 QTRAP hybrid triple quadrupole linear ion trap mass spectrometer (QLIT-MS) with a turbo Ion Spray source (Applied Biosystems), coupled to a Waters Acquity Ultra-Performance™ liquid chromatograph (UPLC). Carbamazepine (CBZ), and iopromide (IPM) were analyzed in electrospray (ESI) positive mode using an Acquity UPLC HSS T3 column (2.1×50 mm, 1.8 μm, Waters) run at 30°C. The eluents employed were acetonitrile with 0.1% formic acid (eluent A), and Milli-Q water with 0.1% formic acid (eluent B) at a flow rate of 0.5 mL min⁻¹. The gradient was started at 2% of eluent A that was increased to 20% A by 3 min, further increased to 50% A by 6 min and further increased to 95% A by 7 min. It was kept constant for 2.5 min, before returning to the initial condition of 2% A by 9.5 min. Triclopyr (TCP) was analyzed in the ESI negative mode using an Acquity UPLC BEH C18 column (2.1×50mm, 1.7μm) from Waters run at 30°C. The eluents for ESI negative mode were mixture of acetonitrile and methanol (1:1, v/v) (eluent A) and 1 mM ammonium acetate (eluent B) at a flow rate of 0.4 mL min⁻¹. The gradient was started at 5% A, further increased to 100% A by 7 min and then kept constant for 2 min, before returning to the initial conditions of 5% A by 9 min.

The target organic contaminants were analyzed in a multiple reaction monitoring (MRM). The source-dependent parameters were: curtain gas, 30 V; nitrogen collision gas, medium; source temperature, 650°C; ion source gases 60 V and 50 V; ion spray voltage, 5500V, and entrance potential 10V. For the negative mode; ion source gases 60 V and 70 V; ion spray voltage, -3500 V, and entrance potential -10V. The optimized compound-dependent MS parameters for each compound are summarized in **Table S1**, and limits of detection and quantification are reported in **Table S2**.

To identify transformation products (TPs) of CBZ, an Orbitrap Exploris 120 equipped with an electrospray ionization source (ESI) was used, operating in positive ionization mode with a voltage of 3500 V. The inject volume of sample was 10 μL , using hypersil GOLDTM column (2.1 \times 50 mm, 1.9 μm , Thermo Fisher Scientific) run at 30°C. The mobile phase consisted of 0.1% formic acid solution (A) and acetonitrile 0.1% formic acid (B) at 0.4 mL min⁻¹. The gradient expressed as the ratio of B was as follows: 0–0.2 min, 2%; a linear increase from 2% to 98%; 0.2–4.75 min, hold at 98% until 6 min, follow by a linear decrease from 98% to 2%; 6–9 min.

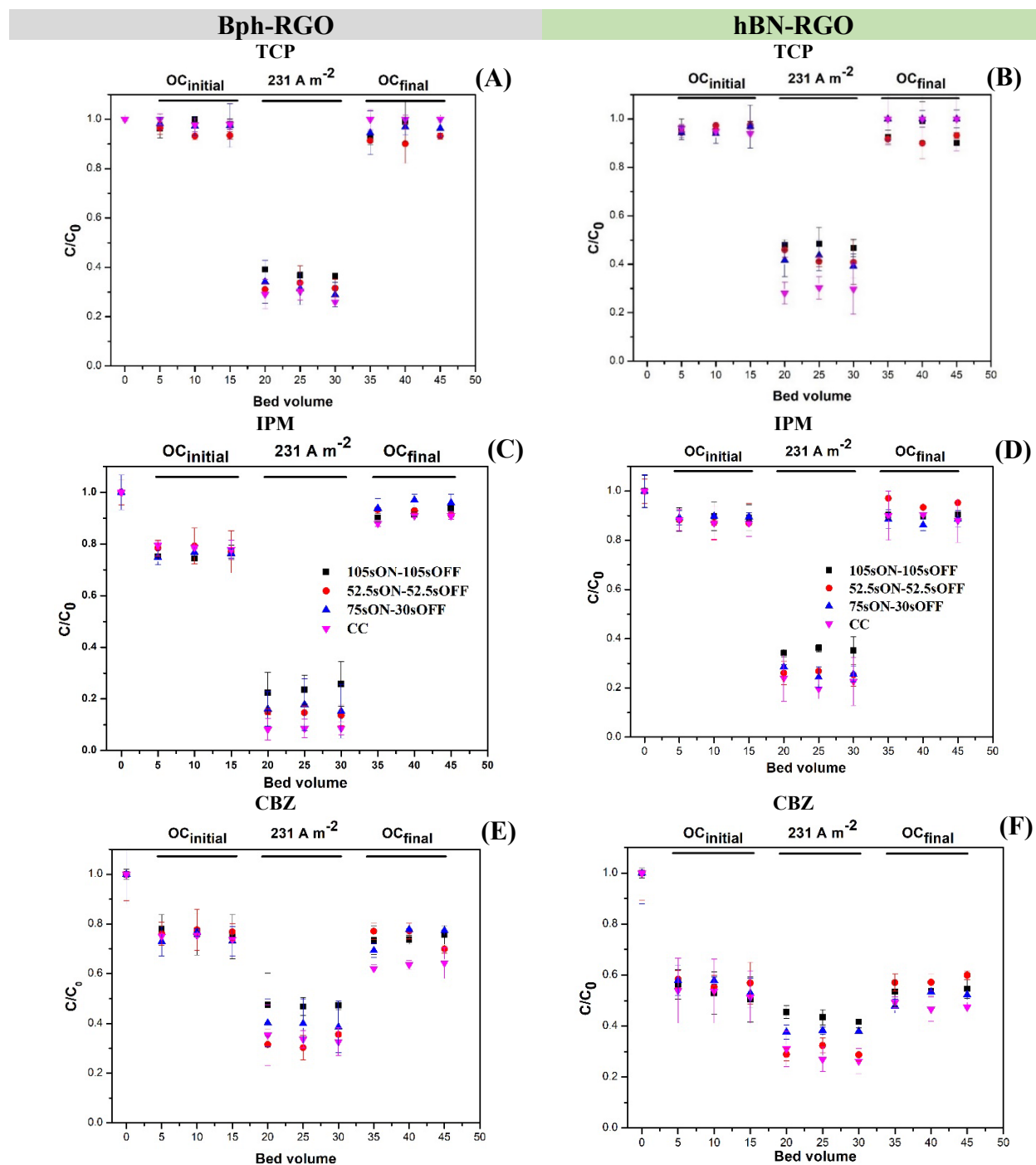


Figure S1. Electrochemical removal of **A-B)** TCP, **C-D)** IPM, and **E-F)** CBZ using Bph-RGO and hBN-RGO anodes respectively, coupled with N-RGO cathode, in the $OC_{initial}$, $231 A m^{-2}$ of applied anodic current at continuous and intermittent mode application with varying durations of ON and OFF cycles, and OC_{final} .

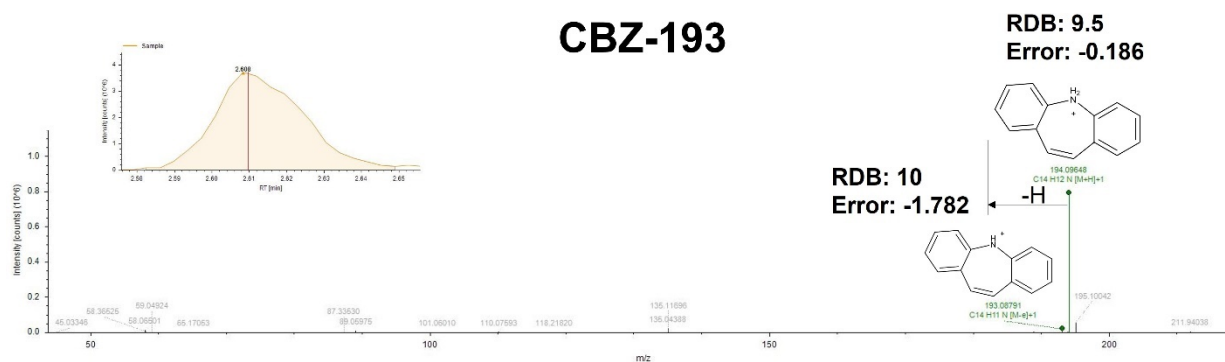


Figure S2. QTRAP MS² mass spectra of the molecular ion CBZ-193 with proposed structures and losses of fragment ions.

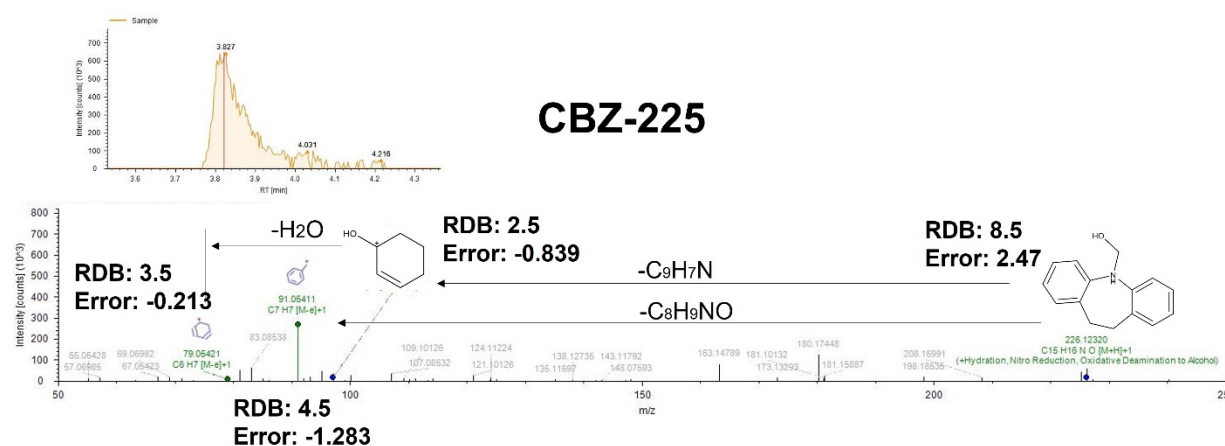


Figure S3. QTRAP MS² mass spectra of the molecular ion CBZ-225 with proposed structures and losses of fragment ions.

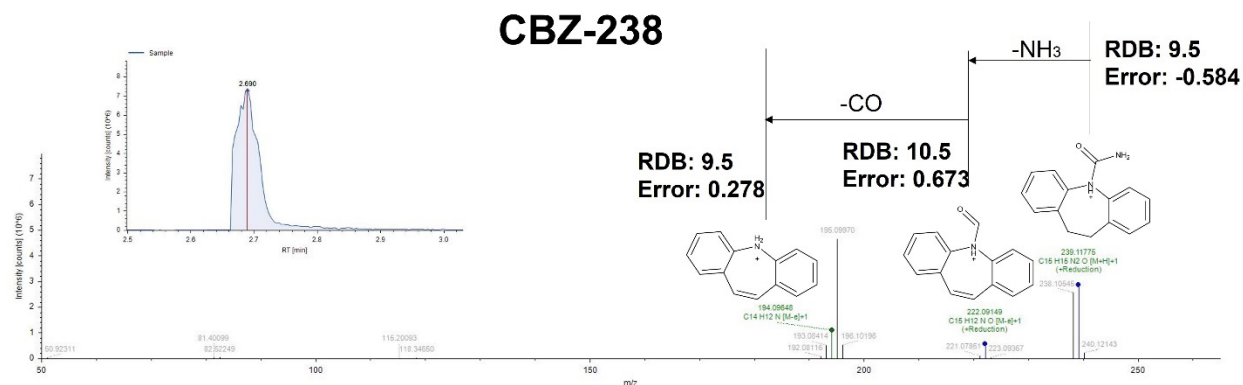


Figure S4. QTRAP MS² mass spectra of the molecular ion CBZ-238 with proposed structures and losses of fragment ions.

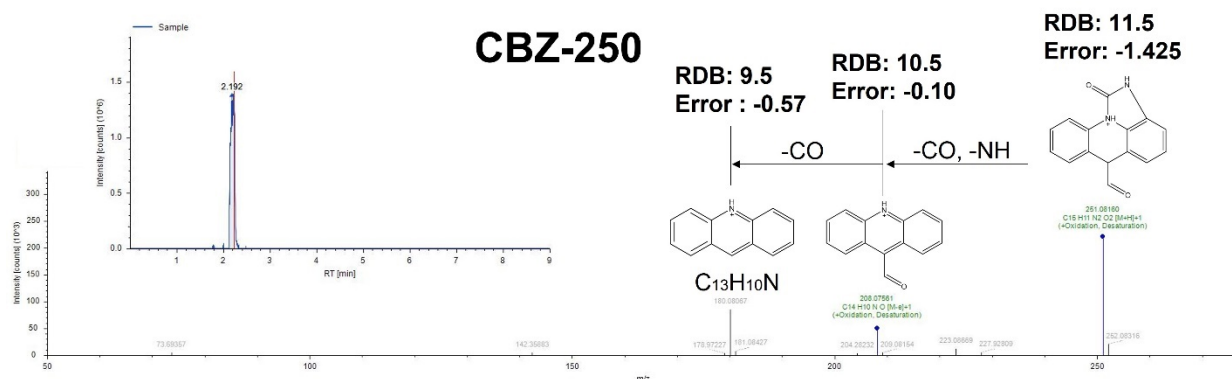


Figure S5. QTRAP MS² mass spectra of the molecular ion CBZ-250 with proposed structures and losses of fragment ions.

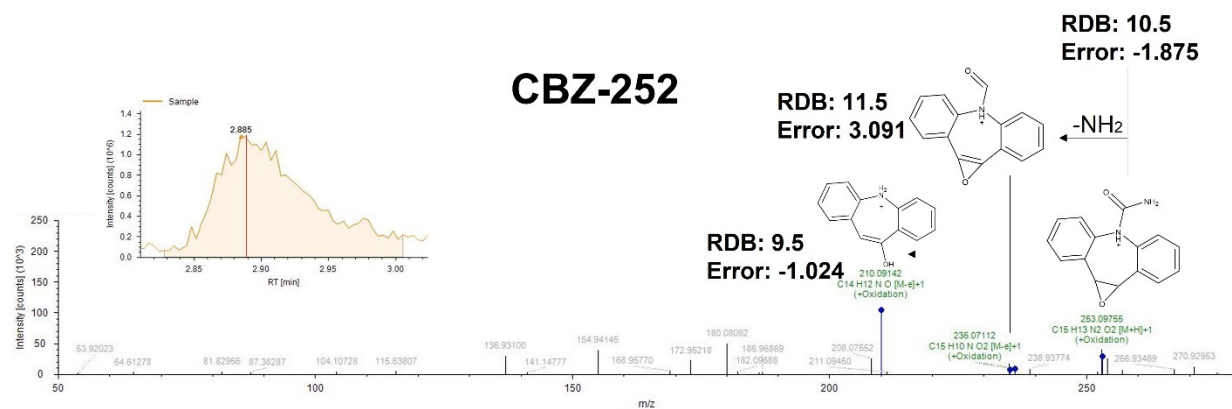


Figure S6. QTRAP MS² mass spectra of the molecular ion CBZ-252 with proposed structures and losses of fragment ions.

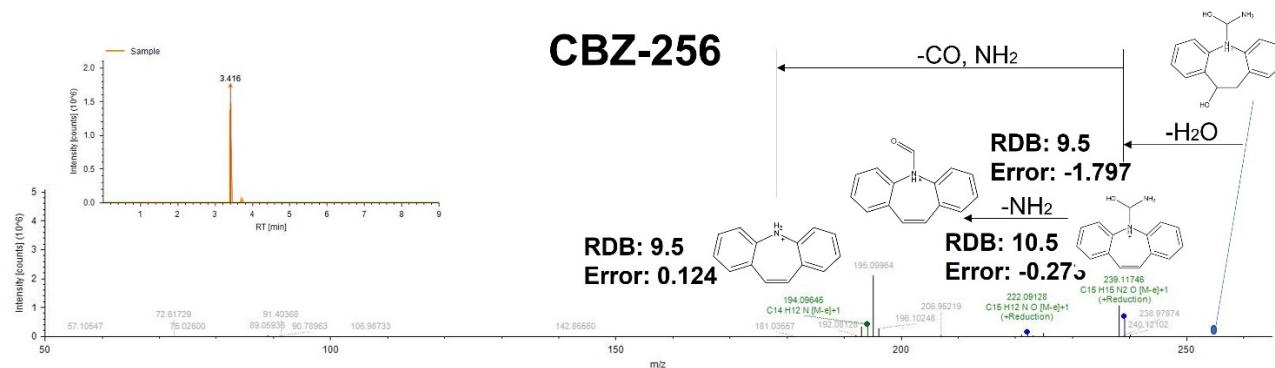


Figure S7. QTRAP MS² mass spectra of the molecular ion CBZ-256 with proposed structures and losses of fragment ions.

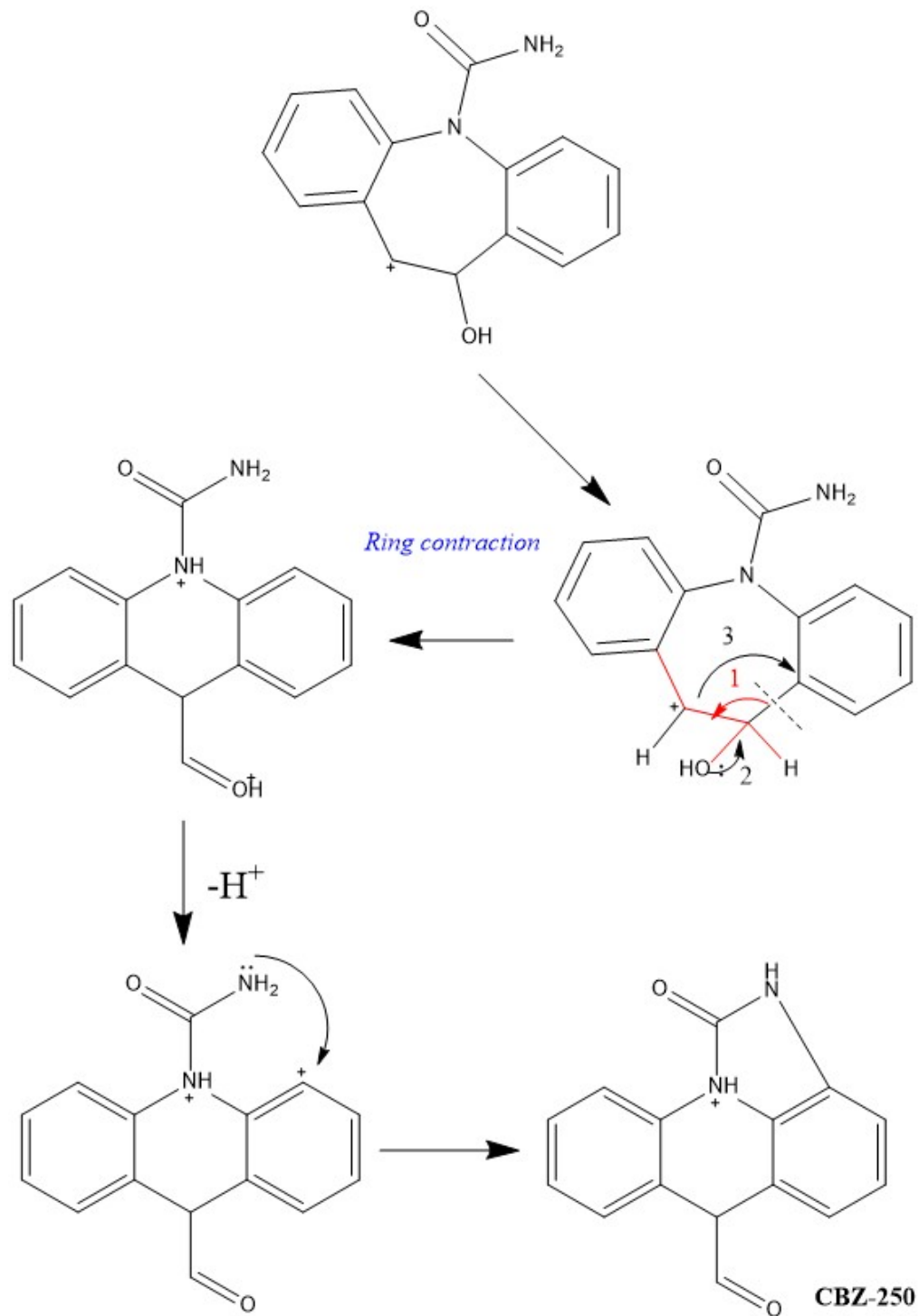


Figure S8. A possible mechanism for transforming CBZ into CBZ-250 involves using an Bph-RGO anode coupled with an N-RGO cathode, operating at 231 A m^{-2} .

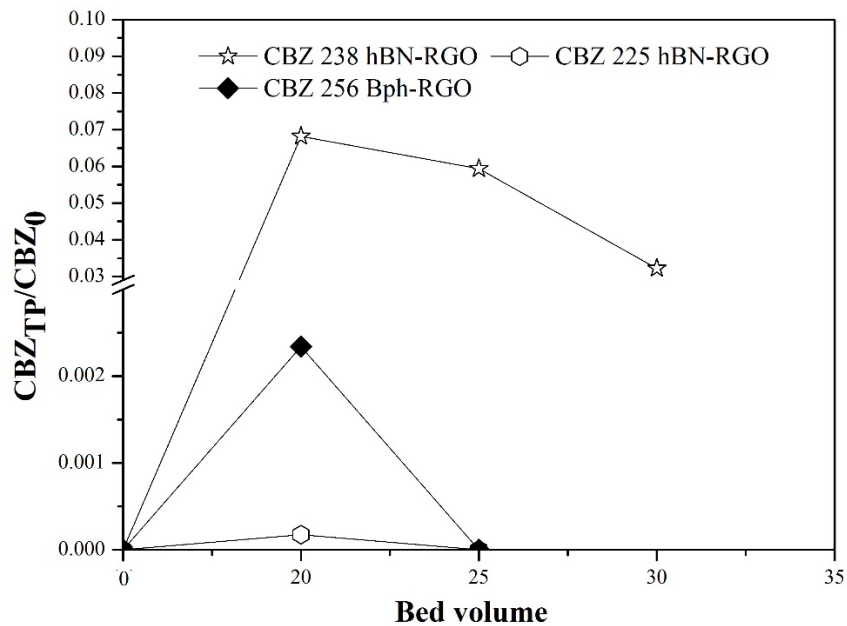
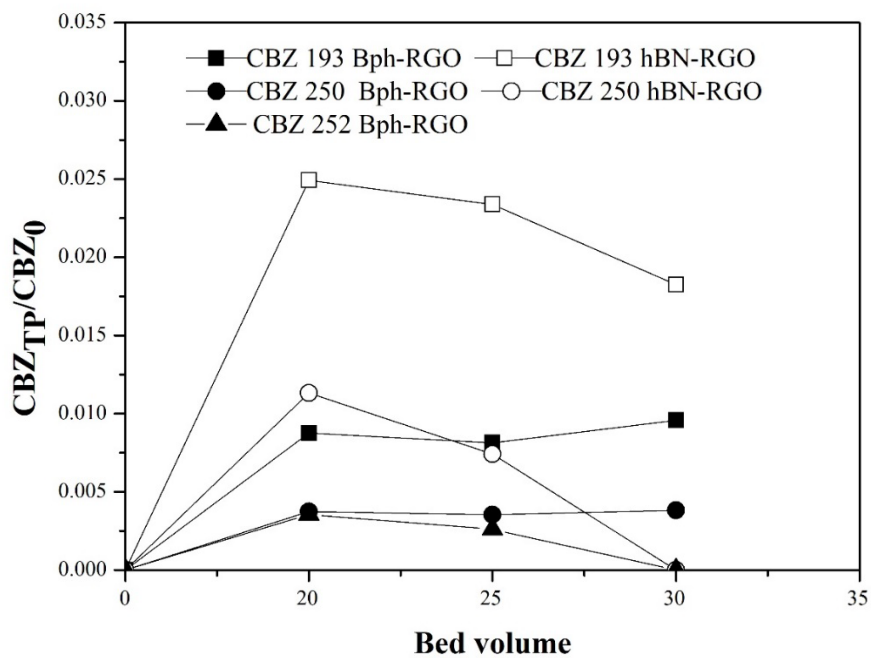


Figure S9. Qualitative profile of TPs identified using Bph-RGO and hBN-RGO anodes each coupled to N-RGO cathode at 231 A m^{-2} .

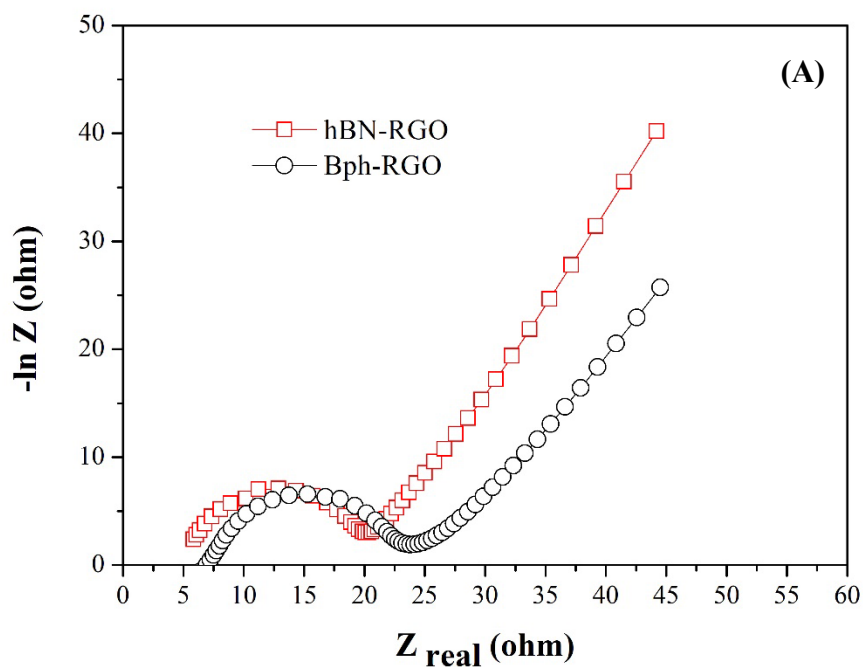


Figure S10. Nyquist plots for Bph- and hBN-RGO anodes in secondary treated wastewater effluent as supporting electrolyte (1.2 mS cm^{-1}).

Table S1. Characteristics of the secondary treated wastewater effluent.

Parameter	Value
pH	7.0
Conductivity (mS/cm)	1.2
PO_4^{3-} (mg/L)	0.57
Cl^- (mg/L)	210.15
SO_4^{2-} (mg/L)	77.92
Na^+ (mg/L)	158.11
NH_4^+ (mg/L)	0.0077
K^+ (mg/L)	29.97
Mg^{2+} (mg/L)	12.82
Ca^+ (mg/L)	89.99

Table S2. The optimized compound-dependent MS parameters: declustering potential (DP), collision energy (CE) and cell exit potential (CXP) for each compound and each transition of the negative and positive mode.

Organic compound	Q1 Mass (Da)	Q3 Mass (Da)	DP	CE	CXP
Carbamazepine	237.01	194.1	156	47	10
	231.01	193	156	47	10
Iopromide	791.72	572.9	156	35	20
	791.72	300.0	156	83	10
Triclopyr	256.18	197.7	-75	-16	-5
	254.01	196	-55	-30	-10

Table S3. Limits of detection (LOD) and quantification (LOQ) of model contaminants using 5500 QTRAP hybrid triple quadrupole linear ion trap mass spectrometer (QLIT-MS).

Compound	LOD (μM)	LOQ (μM)
Carbamazepine (CBZ)	0.03	0.09
Iopromide (IPM)	0.006	0.02
Triclopyr (TCP)	0.002	0.008

Table S4. Parameters of the electrochemical circuit fitted with experimental Nyquist diagrams for all anodes in the low conductivity electrolyte (10 mM phosphate buffer at pH 7, 1 mS cm⁻¹).

Equivalent circuit: R1+C2/R2+Q3/(R3+Q4)			
	RGO	hBN-RGO	Bph-RGO
R1	9.176 Ohm	8.188 Ohm	7.191 Ohm
C2	10.47x10 ¹² F	5.171x10 ⁻⁶ F	0.288x ⁻⁶ F
R2	19.359 Ohm	14.12 Ohm	15.3 Ohm
Q3	2.487x10 ⁻⁶ F.s ^(a - 1)	0.400 6x10 ⁻³ F.s ^(a - 1)	1.133x10 ⁻³ F.s ^(a - 1)
R3	19.47 Ohm	19.36 Ohm	13.92 Ohm
Q4	1.131x10 ⁻³ F.s ^(a - 1)	0.904 2x10 ⁻³ F.s ^(a - 1)	2.471x10 ⁻³ F.s ^(a - 1)

Table S5. Chemical structures with represented charge at neutral pH, and physico-chemical properties of the target contaminants: molecular weight (MW), pKa, octanol-water distribution coefficient calculated based on chemical structure at pH 7.4 (ACD/logD), and polar surface area. The calculation of Van der Waals volume was performed using the methodology developed by Zhao et al. [1], and other information was obtained from <https://chemicalize.com/>

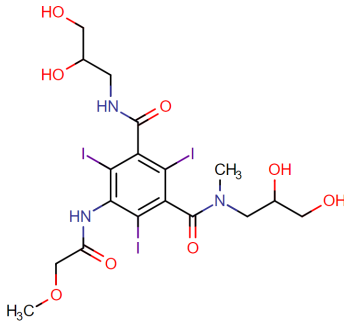
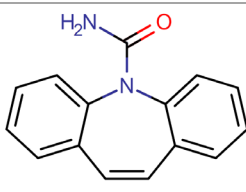
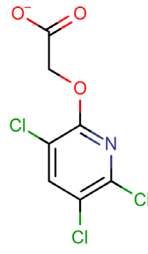
Organic compound MW (g mol ⁻¹)	Chemical structure	pka	logD	Polar surface area (Å ²)
Iopromide (791.11)		11.1	-2.1	169
Carbamazepine (236.27)		15.96	2.3	46
Triclopyr (256.46)		2.28	-1.0	59

Table S6. Reported bimolecular rate constants of target contaminants with ozone and hydroxyl radicals at neutral pH.

Compound	K_{O_3} ($M^{-1} s^{-1}$)	$k_{HO\cdot}$ ($M^{-1} s^{-1}$)
Iopromide	93.07 [2]	3.34×10^9 [3]
Triclopyr	105 [4]	1.7×10^9 [4]
Carbamazepine	9.1×10^5 [5]	9.1×10^9 [6]

Table S7. Ohmic-drop corrected potentials for RGO, Bph-RGO and hBN-RGO anode vs Standard Hydrogen Electrode (SHE) at 231 A m^{-2} for the three electrochemical systems and wastewater-WW (current density, 115 Am^{-2}).

	Matrix	Recorded anodic potential (V/SHE)				Ohmic-drop corrected anodic potential (V/SHE)			
		CC	52.5s ON	105s ON	75s ON 30s OFF	CC	52.5s ON	105s ON 105s OFF	75s ON 30s OFF
RGO	PB	8.2	8.9	8.9	9.1	4.5	5.3	5.3	5.5
Bph-RGO	PB	6	8.7	7.9	9.0	3.1	5.8	5.1	6.1
hBN-RGO	PB	7	8.9	8.9	9.1	3.7	5.6	5.6	5.8
Bph-RGO	WW	6	6.5			4.6	5.1		
hBN-RGO	WW	5	5.5	--	--	3.4	3.9	--	--

Table S8. Degradation kinetic constant k (min^{-1}) of target contaminants on different anodes sponges electrodes.

	RGO				hBN-RGO				Bph-RGO			
	105/ 105	52.5/ 52.5	75/ 30	CC	105/ 105	52.5/ 52.5	75/ 30	CC	105/ 105	52.5/ 52.5	75/ 30	CC
IPM	0.12	0.15	0.16	0.16	0.19	0.21	0.21	0.22	0.22	0.24	0.24	0.27
CBZ	0.08	0.09	0.10	0.14	0.16	0.20	0.18	0.21	0.17	0.19	0.15	0.19
TCP	0.12	0.13	0.14	0.13	0.15	0.16	0.16	0.20	0.19	0.18	0.20	0.20

Table S9. Electric energy consumption (kWh m^{-3}) for the removal of target compounds in the experiments with continuous and intermittent current application in 10 mM phosphate buffer-PB (current density, 231 Am^{-2}) and wastewater-WW (current density, 115 Am^{-2}).

	CC (kWh m^{-3})	52.5s ON/52.5s OFF (kWh m^{-3})	105s ON/105s OFF (kWh m^{-3})	75s ON/30s OFF (kWh m^{-3})
RGO	27.1	11.5	11.5	15.6
Bph-RGO (PB)	24.8	13.5	13.1	18.3
hBN-RGO (PB)	23.6	11.7	11.7	15.8
Bph-RGO (WW)	9.3	4.4	--	--
hBN-RGO (WW)	6.9	3.6	--	--

Table S10. Electrochemical oxidation of CBZ, IPM, and TCP by boron-doped diamond electrodes (BDD)

Target compound	Boron-doped diamond electrodes (BDD)							RGO-based electrodes (Our study)		
	C ₀ of contaminants and employed electrolyte	Current density and flow	Reactor	Removal (%)	Rate constant	Energy consumption (kWhm ⁻³)	Ref	Removal (%)	Rate constant	Energy consumption (kWhm ⁻³)
CBZ	10 mg L ⁻¹ in Na ₂ SO ₄ (400 mg L ⁻¹)	5.4 mA/cm ² 232 mL/min	Continuous mode	81.52	0.07 min ⁻¹	44	[7]	28-72	0.08-0.21 min ⁻¹	Continuous: 24-27 Intermittent: 12-14 Real stream: 7-9
	100 µg L ⁻¹ in Different aqueous matrices with high conc of Cl ⁻	100 mA/cm ²	Batch-stirred reactor	>92	0.016 min ⁻¹	70	[8]			
	2.11×10 ⁻⁴ mol L ⁻¹ in 0.48 M Na ₂ SO ₄	190 mA/cm ² 1.25 mL/min	Continuous mode	100	n.i	n.i	[9]			
	50 mM NaClO ₄	10 mA/cm ²	Batch mode	100	0.0027-0.312 min ⁻¹	n.i	[10]			
	0.44 Mm in 100 mM phosphate buffer	120 mA/cm ²	Batch mode	100	n.i	n.i	[11]			
	2 µg L ⁻¹ in	200 A m ⁻²	Batch mode	100	2.4-29.4 h ⁻¹	2.44-45.6	[12]			

	Na ₂ SO ₄ (40 mM) and, NaNO ₃ (60 mM)	200 mL/min							
IPM	20 µg L ⁻¹ in Na ₂ SO ₄ and NaNO ₃ anolytes	15 mA/cm ² 370 mL/min	Batch mode	75	0.10 h ⁻¹	1.44	[13]	42-93	0.12-0.27 min ⁻¹
	5 mg L ⁻¹ in Simulated wastewater	4.8 mA/cm ² 250 L h	Continuous mode	33	0.0019-0.0023 min ⁻¹	n.i	[14]		
	15 - 25 mg/L in 0.01M Na ₂ SO ₄	0.31 mA/cm ²	Batch mode	96	0.3*10 ⁻⁴ s ⁻¹	n.i	[15]		
	2 µg L ⁻¹ in Na ₂ SO ₄ (40 mM) and, NaNO ₃ (60 mM)	200 A m ⁻² 200 mL/min	Batch mode	100	0.83-11.9 h ⁻¹	2.44-45.6	[12]		
TCP	0.12 mM in 0.050 M Na ₂ SO ₄	16 mA/cm ²	Batch mode	78	0.048 min ⁻¹	66.8	[16]	43-72	0.12-0.20 min ⁻¹
	100 µg L ⁻¹ in secondary effluent	196 A m ⁻² 162 mL/min	Batch mode	40	0.0038 min ⁻¹	1.92 kW h m ⁻³ - 2.56 kW h m ⁻³	[17]		
	2 µg L ⁻¹ in Na ₂ SO ₄ (40 mM) and, NaNO ₃ (60 mM)	200 A m ⁻² 200 mL/min	Batch mode	100	1.3-13.6 h ⁻¹	2.44-45.6	[12]		

n.i= information not reported or insufficient to calculate.

Table S11. List of the transformation products using hBN-RGO and Bph-RGO (anode) coupled with N-RGO (cathode)

Name	Formula	RT (min)	Calc. MW	m/z	Error (ppm)	Reported in other studies
CBZ	C ₁₅ H ₁₂ N ₂ O	2.66	236.0947	236.0948	-0.87	
CBZ-193	C ₁₄ H ₁₁ N	2.60	193.0889	194.0965	-0.18	[18]
CBZ-225	C ₁₅ H ₁₅ NO	3.82	226.0928	226.1232	2.48	[18]
CBZ-238	C ₁₅ H ₁₄ N ₂ O	2.69	238.111	239.118	-0.58	[19]
CBZ-250	C ₁₅ H ₁₀ N ₂ O ₂	2.23	250.0739	251.0816	-1.43	[18,20]
CBZ-252	C ₁₅ H ₁₂ N ₂ O ₂	2.89	252.0897	253.0975	-1.86	[18]
CBZ-256	C ₁₅ H ₁₆ N ₂ O ₂	3.41	256.1208	239.1175	-1.55	

References

- [1] Y.H. Zhao, M.H. Abraham, A.M. Zissimos, Fast calculation of van der Waals volume as a sum of atomic and bond contributions and its application to drug compounds, *J. Org. Chem.* 68 (2003) 7368–7373. <https://doi.org/10.1021/jo034808o>.
- [2] B. Ning, N.J. Graham, Ozone degradation of iodinated pharmaceutical compounds, *J. Environ. Eng.* 134 (2008) 944–953. [https://doi.org/10.1061/\(ASCE\)0733-9372\(2008\)134:12\(944\)](https://doi.org/10.1061/(ASCE)0733-9372(2008)134:12(944)).
- [3] J. Jeong, J. Jung, W.J. Cooper, W. Song, Degradation mechanisms and kinetic studies for the treatment of X-ray contrast media compounds by advanced oxidation/reduction processes, *Water Res.* 44 (2010) 4391–4398. <https://doi.org/10.1016/j.watres.2010.05.054>.
- [4] F.J. Beltrán, A. Rey, Free radical and direct ozone reaction competition to remove priority and pharmaceutical water contaminants with single and hydrogen peroxide ozonation systems, *Ozone Sci. Eng.* 40 (2018) 251–265. <https://doi.org/10.1080/01919512.2018.1431521>.
- [5] D.C. McDowell, M.M. Huber, M. Wagner, U. Von Gunten, T.A. Ternes, Ozonation of carbamazepine in drinking water: identification and kinetic study of major oxidation products, *Environ. Sci. Technol.* 39 (2005) 8014–8022. <https://doi.org/10.1021/es050043l>.
- [6] Y. Zhang, H. Wang, Y. Li, B. Wang, J. Huang, S. Deng, G. Yu, Y. Wang, Removal of micropollutants by an electrochemically driven UV/chlorine process for decentralized water treatment, *Water Res.* 183 (2020) 116115. <https://doi.org/10.1016/j.watres.2020.116115>.
- [7] C. García-Gómez, P. Drogui, F. Zaviska, B. Seyhi, P. Gortáres-Moroyoqui, G. Buelna, C. Neira-Sáenz, M. Estrada-Alvarado, R.G. Ulloa-Mercado, Experimental design methodology applied to electrochemical oxidation of carbamazepine using Ti/PbO₂ and Ti/BDD electrodes, *J. Electroanal. Chem.* 732 (2014) 1–10. <https://doi.org/10.1016/j.jelechem.2014.08.032>.
- [8] B.M. de Souza-Chaves, M. Bosio, M. Dezotti, M.E. Quinta-Ferreira, R.M. Quinta-Ferreira, E.M. Saggiaro, Advanced electrochemical oxidation applied to benzodiazepine and carbamazepine removal: Aqueous matrix effects and neurotoxicity assessments employing rat hippocampus neuronal activity, *J. Water Process Eng.* 49 (2022) 102990. <https://doi.org/10.1016/j.jwpe.2022.102990>.
- [9] J.R. Domínguez, T. González, P. Palo, J. Sánchez-Martín, Electrochemical advanced oxidation of carbamazepine on boron-doped diamond anodes. Influence of operating variables, *Ind. Eng. Chem. Res.* 49 (2010) 8353–8359. <https://doi.org/10.1021/ie101023u>.
- [10] H. Song, L. Yan, J. Jiang, J. Ma, Z. Zhang, J. Zhang, P. Liu, T. Yang, Electrochemical activation of persulfates at BDD anode: Radical or nonradical oxidation?, *Water Res.* 128 (2018) 393–401. <https://doi.org/10.1016/j.watres.2017.10.018>.
- [11] M. Pierpaoli, A. Dettlaff, M. Szopińska, K. Karpieńko, M. Wróbel, A. Łuczkiwicz, S. Fudala-Książek, R. Bogdanowicz, Simultaneous opto-electrochemical monitoring of carbamazepine and its electro-oxidation by-products in wastewater, *J. Hazard. Mater.* 419 (2021) 126509. <https://doi.org/10.1016/j.jhazmat.2021.126509>.
- [12] A. Farhat, J. Keller, S. Tait, J. Radjenovic, Removal of persistent organic contaminants by electrochemically activated sulfate, *Environ. Sci. Technol.* 49 (2015) 14326–14333. <https://doi.org/10.1021/acs.est.5b02705>.
- [13] J. Radjenovic, M. Petrovic, Sulfate-mediated electrooxidation of X-ray contrast media on boron-doped diamond anode, *Water Res.* 94 (2016) 128–135. <https://doi.org/10.1016/j.watres.2016.02.045>.

- [14] G. Loos, T. Scheers, K. Van Eyck, A. Van Schepdael, E. Adams, B. Van der Bruggen, D. Cabooter, R. Dewil, Electrochemical oxidation of key pharmaceuticals using a boron doped diamond electrode, *Sep. Purif. Technol.* 195 (2018) 184–191. <https://doi.org/10.1016/j.seppur.2017.12.009>.
- [15] A.L. Schneider, S. Tisler, H. Schell, T. Matthée, B. Behrendt-Fryda, A. Tiehm, Electrochemical oxidation of iodinated X-ray contrast media by boron-doped diamond electrodes, *Desalin. Water Treat.* 91 (2017) 268–272.
- [16] I.C. Da Costa Soares, R. Oriol, Z. Ye, C.A. Martínez-Huitle, P.L. Cabot, E. Brillas, I. Sirés, Photoelectro-Fenton treatment of pesticide triclopyr at neutral pH using Fe (III)–EDDS under UVA light or sunlight, *Environ. Sci. Pollut. Res.* 28 (2021) 23833–23848. <https://doi.org/10.1007/s11356-020-11421-8>.
- [17] S. Garcia-Segura, J. Keller, E. Brillas, J. Radjenovic, Removal of organic contaminants from secondary effluent by anodic oxidation with a boron-doped diamond anode as tertiary treatment, *J. Hazard. Mater.* 283 (2015) 551–557. <https://doi.org/10.1016/j.jhazmat.2014.10.003>.
- [18] A. Ghauch, H. Baydoun, P. Dermesropian, Degradation of aqueous carbamazepine in ultrasonic/Fe⁰/H₂O₂ systems, *Chem. Eng. J.* 172 (2011) 18–27. <https://doi.org/10.1016/j.cej.2011.04.002>.
- [19] A. König, C. Weidauer, B. Seiwert, T. Reemtsma, T. Unger, M. Jekel, Reductive transformation of carbamazepine by abiotic and biotic processes, *Water Res.* 101 (2016) 272–280. <https://doi.org/10.1016/j.watres.2016.05.084>.
- [20] H. Yin, Q. Zhang, Y. Su, Y. Tang, M. Zhou, A novel UV based advanced oxidation process with electrochemical co-generation of chlorine and H₂O₂ for carbamazepine abatement: better performance, lower energy consumption and less DBPs formation, *Chem. Eng. J.* 425 (2021) 131857. <https://doi.org/10.1016/j.cej.2021.131857>.